arXiv:1409.0866v2 [astro-ph.GA] 8 Dec 2014

The Dynamical Evolution of Stellar Black Holes in Globular Clusters

Meagan Morscher[1,2], Bharath Pattabiraman[1,3], Carl Rodriguez[1,2], Frederic A. Rasio[1,2], and Stefan Umbreit[1,2]

Center for Interdisciplinary Exploration and Research in Astrophysics (CIERA), Northwestern University, Evanston, IL, USA

Department of Physics and Astronomy, Northwestern University, Evanston, IL, USA

Department of Electrical Engineering and Computer Science, Northwestern University, Evanston, IL, USA

m.morscher@u.northwestern.edu

ABSTRACT

Our current understanding of the stellar initial mass function and massive star evolution suggests that young globular clusters may have formed hundreds to thousands of stellar-mass black holes, the remnants of stars with initial masses from $\sim 20 - 100\,M_{\odot}$. Birth kicks from supernova explosions may eject some black holes from their birth clusters, but most should be retained. Using a Monte Carlo method we investigate the long-term dynamical evolution of globular clusters containing large numbers of stellar black holes. We describe numerical results for 42 models, covering a range of realistic initial conditions, including up to 1.6×10^6 stars. In almost all models we find that significant numbers of black holes (up to $\sim 10^3$) are retained all the way to the present. This is in contrast to previous theoretical expectations that most black holes should be ejected dynamically within a few Gyr. The main reason for this difference is that core collapse driven by black holes (through the Spitzer "mass segregation instability") is easily reverted through three-body processes, and involves only a small number of the most massive black holes, while lower-mass black holes remain well-mixed with ordinary stars far from the central cusp. Thus the rapid segregation of stellar black holes does not lead to a long-term physical separation of most black holes into a dynamically decoupled inner core, as often assumed previously. Combined with the recent detections of several black hole X-ray binary candidates in Galactic globular clusters, our results suggest that stellar black holes could still be present in large numbers in many globular clusters today, and that they may play a significant role in shaping the long-term dynamical evolution and the present-day dynamical structure of many clusters.

Subject headings: binaries: close — globular clusters: general — Gravitational waves — Methods: numerical — Stars: black holes — Stars: kinematics and dynamics

1. Introduction

Massive star clusters ($M \gtrsim 10^4\,M_\odot$) should form $\sim 100 - 1000$ stellar-mass black holes (BHs) through normal stellar evolution, and, as long as BH birth kicks are sufficiently low, most should be retained initially in the cluster (Belczynski et al. 2006; Willems et al. 2005; Wong et al. 2012). With masses of $\sim 10\,M_\odot$, the BHs quickly segregate toward the dense central region of the cluster where they interact dynamically to form binaries with either a normal star or another compact remnant as a companion. These binaries can evolve to produce X-ray binaries (XRBs) or merging compact object binaries potentially detectable by future ground-based gravitational wave (GW) observatories (LIGO, VIRGO; Harry et al. 2010; The Virgo Collaboration 2014). These systems could be found either inside clusters or in the field after being dynamically ejected. It is well known that the formation rate per unit mass of XRBs is orders of magnitude larger in massive clusters than it is in the field (e.g., Pooley et al. 2003), which suggests that stellar dynamics must play an essential role in producing XRBs in present-day clusters.

For several decades, observations, theoretical arguments, and simulations have all suggested that old globular clusters (GCs) should have very few (perhaps ~ 1) BHs remaining at present. While many XRBs had been discovered in Galactic GCs (Grindlay et al. 2001), they had all been clearly identified as accreting neutron stars (NS) (see Kalogera et al. 2004, and references therein). Furthermore, there were no good candidates for BHs in extragalactic GCs (for a review of GC X-ray sources as of 2006, see Verbunt & Lewin 2006). The absence of BHs from GCs was explained with simple theoretical arguments based on the prediction that all BHs should rapidly concentrate near the cluster center through dynamical friction from the low-mass background stars (Kulkarni et al. 1993; Sigurdsson & Hernquist 1993). Eventually the BHs would succumb to the so-called Spitzer "mass-segregation instability" (Spitzer 1969; Kulkarni et al. 1993; Watters et al. 2000) and form a very dense subsystem within the cluster core that consists primarily of BHs and is dynamically decoupled from the other stars. The small-N sub-cluster of BHs has a very short relaxation time, so it should promptly undergo its own core collapse, begin to form hard binaries through three-body interactions, and subsequently eject single and binary BHs. This sub-system should then completely evaporate within at most a few Gyr, leaving behind a GC essentially devoid of BHs well before reaching the ~ 10 Gyr ages typical of Galactic GCs. Several other theoretical studies later confirmed these predictions through numerical simulations (e.g., Portegies Zwart & McMillan 2000, O'Leary et al. 2006, Banerjee et al. 2010).

Over the last few years, however, our understanding of BHs in dense star clusters has taken a dramatic turn. The old story began to change when the first BH XRB candidate was identified inside an old GC in the Galaxy NGC 4472 (Maccarone et al. 2007). Several more BH candidates have subsequently been discovered in extragalactic GCs (e.g., Barnard et al. 2011; Maccarone et al. 2011; Shih et al. 2010). Recently, Strader et al. (2012) discovered *two* BHs inside of the Galactic GC M22. These stellar BH candidates are the first ever to be identified in a Milky Way GC, as well as the first to be discovered through radio observations. By assuming that these systems are BH–white-dwarf (WD) binaries, Strader et al. were able to use published theoretical models by

Ivanova et al. (2010) to estimate the fraction of present-day BHs in GCs that are actively accreting from a WD companion. They estimate that the detection of two accreting BHs in M22 implies a total number of $\sim 5 - 100$ BHs. The same group recently found another BH in a different galactic GC, M62, also through radio observations (Chomiuk et al. 2013). Several additional candidates may soon be added to this list (Strader, private communication).

On the theoretical side, several recent studies have provided hints that old clusters might actually be able to retain significant numbers of BHs. Mackey et al. (2008) used N-body simulations of clusters with BHs to explain the trend of increasing spread in core radius with cluster age that is observed in the Magellanic Clouds. They found that a population of retained BHs could provide a heat source for some clusters, offering a possible explanation for the observed spread in the radii of Magellanic Cloud clusters. In some of their models, significant numbers of BHs (as many as ~ 100) were retained for ~ 10 Gyr. Sippel & Hurley (2013) presented a scaled-down direct N-body model of M22. At an age of 12 Gyr, their model contains 16 BHs (about 1/3 of the initially-retained population), which is consistent with the prediction of Strader et al. (2012). Our own preliminary Monte Carlo study by Morscher et al. (2013) suggested that some clusters may retain as many as hundreds of BHs for 12 Gyr. The long-term survival of such a large number of BHs is explained by the fact that the BHs do not become Spitzer unstable on the whole, but instead the majority of the BHs remain well mixed with the rest of the cluster throughout the entire 12 Gyr evolution.

A very different study by Breen & Heggie (2013) focused on the evolution of two-component clusters consisting of a population of BHs co-existing within a background cluster of low-mass stars. They provide analytic calculations as well as direct N-body simulations which both suggest that the flow of energy between the sub-cluster of BHs and the rest of the stars is ultimately determined by the cluster as a whole. From this it follows that the rate of energy production in the BH subsystem, as well as its evaporation rate, is also regulated by the whole cluster. This implies that BHs can be retained for much longer than previously thought (i.e., for $\sim 10\, t_{\rm rh,i}$, where $t_{\rm rh,i}$ is the initial half-mass relaxation timescale) because their dynamical evolution happens on the evolutionary timescale of the whole cluster, as opposed to that of the BH subsystem. This suggests that the long-standing assumption that BHs actually decouple from clusters, which is the basis for the argument that old clusters should be deplete of BHs, may no longer hold true.

While the theoretical arguments presented in Breen & Heggie (2013) are interesting and suggestive, these two-component models cannot be directly compared to real GCs, which have a broad spectrum of stellar and BH masses, as well as larger total cluster masses. Several more-realistic studies have now predicted the survival of at least some BHs (e.g., Heggie & Giersz 2014; Mackey et al. 2008; Morscher et al. 2013; Sippel & Hurley 2013), but there is still no definitive answer as to *how many* might actually be hiding in old GCs at present, nor whether models that do retain many BHs will look like observed Galactic GCs. The answers to these questions can help to constrain the initial populations of BHs and BH kicks, both of which are still highly uncertain (Farr et al. 2011; Janka 2013; Repetto et al. 2012). For these reasons, the topic of stellar BHs in clusters is worthy of further theoretical study.

In this paper, we present a large grid of Monte Carlo simulations of realistic, large-N, Milky-Way-like GCs and address the question of retention of BHs in clusters and the dynamical evolution of clusters with BHs. We are most interested in understanding whether clusters can retain significant numbers of BHs all the way to present and still have observable properties similar to the GCs in our own Galaxy. Our focus, therefore, is on clusters that initially retain most of the BHs that form, under the assumption that BHs receive small birth kicks (compared to NSs; See Section 2.1). This work has been made possible by the recent parallelization of our code, which has provided the speed up necessary to simulate star clusters with up to $\sim 10^6$ stars, large populations of BHs, and realistic stellar physics (Pattabiraman et al. 2013). The rest of this paper is organized as follows. In Section 2 we give an overview of our computational method, including a new comparison with a direct N-body study focusing on BHs. We provide the initial conditions that we have used for our calculations in Section 3. The results of our 42 simulations are described in detail in Section 4. Finally in Section 5 we summarize our results, compare to previous studies, discuss the uncertainties in our assumptions, and give our conclusions.

2. Monte Carlo Method

2.1. Overview of Method

We use a Monte Carlo (MC) method for modeling the dynamical evolution of GCs. While the direct N-body method is more accurate than MC schemes, it can only simulate clusters with up to $N \sim 10^5$ due to the poor scaling with N (computation time $\sim N^3/\log N$). In order to model large MW GCs with initial N up to $\sim 10^6$, and to cover the large parameter space of relevant initial conditions, we must employ a more approximate technique. In MC methods, the computation time scales as $\sim N \log N$, which makes it feasible to model realistic GCs and to study the evolution of rare objects, such as BHs.

Our MC implementation is a variation of the so-called "orbit-averaged Monte Carlo method" developed by Hénon (1971) for solving the Fokker-Planck equation. The details of our method are described in many previous studies (Joshi et al. 2000, 2001; Fregeau et al. 2003; Fregeau & Rasio 2007; Chatterjee et al. 2010; Umbreit et al. 2012) where we have also shown our results to be in excellent agreement with direct N-body simulations. Here we highlight the most important details for our study of BHs in clusters. We treat the cluster on a star-by-star basis, which makes it possible to layer on complexity, such as stellar evolution and strong binary interactions. Stars and binaries are evolved according to the stellar evolution fitting formulae and interacting binary evolution calculations of SSE and BSE (Hurley et al. 2000, Hurley et al. 2002). We use the modified stellar remnant formation prescription of Belczynski et al. (2002), which is based on the theoretical calculations of Fryer & Kalogera (2001). In this prescription, BHs can form either through "direct collapse" (i.e., with no supernova explosion) or through partial fallback of material that was initially expelled in a supernova explosion, depending on the mass of the stellar core

just before BH formation. The range of initial masses that form BHs, as well as the formation mechanism and the final BH masses, are all dependent on the details of the stellar evolution scheme and metallicity. For $Z = 0.001$, our implementation produces BH masses in the range $\sim 3-30\,M_\odot$. Stars with initial masses $\gtrsim 25\,M_\odot$ directly collapse into BHs at the end of their lifetime, while those with initial masses between $\sim 19-25\,M_\odot$ form BHs through fallback. All NSs and some BHs receive natal kicks assumed to be generated by the asymmetric ejection of mass during a supernova explosion. NS kicks are drawn from a Maxwellian distribution with $\sigma = 265$ km s^{-1}. We assume momentum-conserving kicks, which means that BHs, being significantly more massive than NSs, receive much smaller kicks (if any). We follow the prescription of Belczynski et al. (2002) to reduce the BH kick magnitude (initially drawn from the NS kick distribution) according to the amount of material that falls back onto the final BH after the supernova explosion. In this prescription, BHs that form via direct collapse do not receive any natal kick, as there is no associated explosion. For compact object binaries BSE calculates the orbital evolution due to emission of GW radiation, which is important for tracking the mergers of BH–BH binaries. Once a binary is ejected from the cluster, however, it is no longer evolved with our code, even though these BH–BH binaries can still potentially merge in the field. For these systems, we estimate the merger time using a simplified timescale for GW inspiral in the weak-field limit (Peters 1964) based on the properties at the time of ejection.

In addition to two-body relaxation, it is also important to accurately model the dynamics of *close* binary encounters. We choose strong binary-binary (B-B) and binary-single (B-S) using MC sampling based on the cross-section for a close interaction between the pair of neighboring objects. These interactions are then integrated directly using `Fewbody`, which allows for many important effects within binary systems, such as exchanges, ionization, hardening of binaries, and ejections, all of which are relevant for the evolution of BHs in clusters.

2.2. New Physics: Three-body Binary Formation

We have recently implemented a simplified prescription for three-body binary formation, a process that is expected to produce an important population of hard BH binaries (Kulkarni et al. 1993; Sigurdsson & Hernquist 1993; Portegies Zwart & McMillan 2000; O'Leary et al. 2006; Banerjee et al. 2010), and is therefore extremely important for this study. If three single stars experience a close resonant encounter, it is possible for two of the stars to become gravitationally bound to one another, with the third star carrying away the extra energy. The probability of binary formation is usually quite low, and realistically only becomes significant under the extreme conditions expected at the core of a cluster which has been driven to collapse by a population of BHs. For non-compact stars three-body binary formation is never important, as it would require a density so high that physical collisions would instead have become dominant much earlier (Chernoff & Huang 1996). Therefore we restrict our attention to BHs. In addition, we are only interested in dynamically hard binaries (Fregeau et al. 2006; Heggie 1975), as only those are expected to survive within the cluster

environment.

Our simplified prescription relies on the calculation of the rate at which three neighboring single BHs will form a hard binary. Using the calculated rate and the current timestep, we can estimate the probability that the three-body system will result in binary formation, and then use MC sampling to select which systems will actually form a new binary. Our implementation follows Ivanova et al. (2005), Ivanova et al. (2010), and O'Leary et al. (2006), where the binary formation rate is expressed in terms of the binary hardness ratio (binary binding energy to background star kinetic energy)

$$\eta = \frac{G\, m_1\, m_2}{r_p\, \langle m \rangle\, \sigma^2}. \tag{1}$$

Here m_1 and m_2 are the masses of the two stars assumed to form a binary, r_p is their separation at pericenter, and $\langle m \rangle$ and σ are the local average mass and velocity dispersion.

Keeping both the geometric and gravitational focusing contributions to the cross section, we construct an expression for the rate of binary formation for the selected neighboring three stars. We calculate the rate at which two stars with masses m_1 and m_2 will form a binary with hardness $\eta \geq \eta_{\rm min}$ during a close encounter with a third star of mass m_3 using

$$\begin{aligned}\Gamma(\eta \geq \eta_{min}) = \sqrt{2}\pi^2 G^5 n^2 v_\infty^{-9} \\ \times (m_1+m_2)^5 \eta_{\rm min}^{-5.5}(1+2\eta_{\rm min}) \\ \times \left[1 + 2\eta_{\rm min}\left(\frac{m_1+m_2+m_3}{m_1+m_2}\right)\right],\end{aligned} \tag{2}$$

where n is the local number density and v_∞ is the average relative velocity at infinity, both of which are computed using a subset of nearby stars (see Section 2.3 for details). We only form binaries with $\eta \geq 5 = \eta_{\rm min}$, with the specific value chosen for each new binary from a distribution according to the differential rate, $\mathrm{d}\Gamma/\mathrm{d}\eta$, with lower limit $\eta_{\rm min}$. After a binary is formed, the new properties of all involved objects are calculated from conservation of momentum and energy.

2.3. Comparison with Direct N-body Calculations

The MC approach requires the calculation of local average of several physical quantities. For example, both the physics of three-body binary formation described above and the selection of the relaxation time depend on the local number density, velocity dispersion, and average stellar mass at a specific radius in the cluster (Joshi et al. 2000). However, it is not the case that these averages should be computed over the same number of stars. While three-body binary formation should depend only on the properties of neighboring stars, the relaxation time step must be applied to the entire cluster. We both expect and require three-body binary formation to be more sensitive to local spikes in number density and velocity dispersion than the cluster-wise relaxation time. Therefore, we must adjust the number of stars used for computing these averages, depending on the scale of the physics in question.

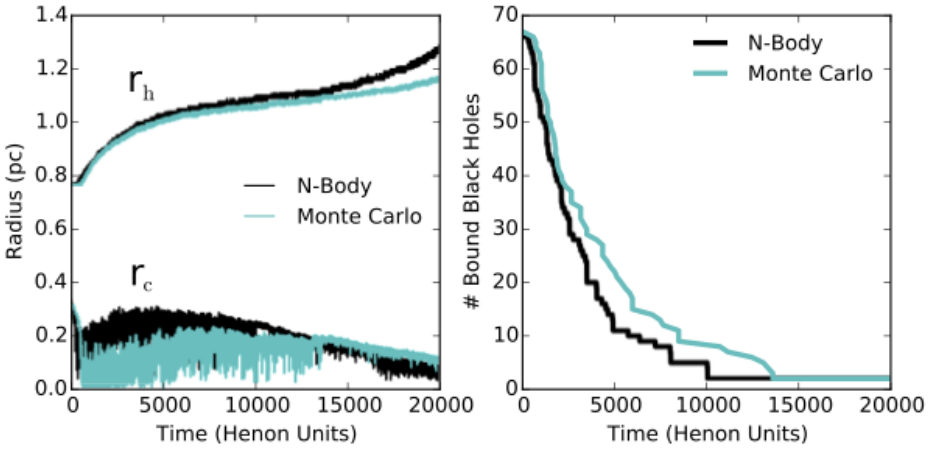

Fig. 1.— Evolution of two-component Plummer models as computed by our Monte Carlo code and the direct N-body code of Breen & Heggie (2013). On the left we show the half-mass radius, $r_{\rm h}$ (top), and core radius, $r_{\rm c}$ (bottom), for the two methods, and on the right, the number of BHs retained in the cluster as a function of time. With the choice of parameters described in Section 2.3 we get good overall agreement with N-body results for the structural properties of our models, and also, crucially, on the BH ejection rate.

As in previous works using our MC code (Joshi et al. 2000, 2001; Fregeau et al. 2003; Fregeau & Rasio 2007; Chatterjee et al. 2010) we determine the optimal code parameters by comparing to direct N-body simulations with identical initial conditions. Since the primary focus of this study is the retention of BHs, we choose for our main test the idealized two-component models recently studied by Breen & Heggie (2013), which provides a simplified description of the evolution of a population of stellar-mass BHs in a cluster. These models are a realization of standard Plummer spheres populated by a large population of low-mass stellar objects and a smaller population of massive objects, considered to be BHs. We consider models with an individual mass ratio of $m_2/m_1 = 20$, and a total cluster mass ratio of $M_2/M_1 = 0.02$, where m_1 and m_2 are the masses of individual particles, and M_1 and M_2 are the total masses of each component. We performed comparison simulations with $64k$ and $128k$ particles, although only the $64k$ runs are illustrated here.

In Figure 1, we compare the cluster properties as reported by the N-body simulations of Breen & Heggie (2013) to those computed by our MC code. Empirically, we find optimal agreement by computing the average quantities over the nearest 40 stars for two-body relaxation, and the nearest 6 stars for three-body binary formation. In particular, the evaporation rate of the BH subcluster in our simulations matches the N-body results very well. Furthermore, we find that our MC approach correctly reproduces the time evolution of the half-mass radius to within 8% after 2×10^5 N-body time units.

Of the measured cluster properties, only the core radius cannot be reproduced perfectly by the MC approach. Immediately following core collapse, the measured core radius for the MC model differs from the N-body results by as much as 65%. This is to be expected: once mass segregation

and core collapse have occurred, the dynamics of the core is primarily driven by the BH subsystem, which has dynamically decoupled from the cluster in these idealized models. Modeling accurately the internal dynamics of a sub-system with $N \sim 100$ particles using an orbit-averaged MC approach is very challenging; however, as the BHs are ejected, and the core becomes populated with a larger number of lower mass stars, the validity of the MC approach is restored, and the core radius better agrees with the direct N-body results. Additionally, the core radius is known to be very sensitive to stochastic physical effects, such as three-body binary formation, so that the agreement between two different models can at best be statistical (Giersz et al. 2008). New techniques are under investigation that will correctly evolve the subcluster dynamics while maintaining the speed of the MC approach. For the present study, we are encouraged by our earlier results presented in Morscher et al. (2013) which suggest that in *realistic* GCs the BHs might actually never decouple from the cluster on the whole, in which case a MC approach is appropriate.

3. Initial Conditions

Using the results of the calibration as described in Section 2.3, we have calculated the dynamical evolution of 42 cluster models with a wide range of initial conditions. All models are initialized as King models (King 1966), with stellar masses chosen in the range $0.1 - 100\,M_\odot$ according to the initial mass function (IMF) of Kroupa (2001), which is a broken power-law of the form $dN/dm \propto m^{-\alpha}$, with $\alpha = 1.3$ for $0.08 \leq m/M_\odot < 0.5$, and $\alpha = 2.3$ for $m/M_\odot \geq 0.5$. Once the single stars are drawn from the IMF, we randomly choose N_b stars to be the primary member of a binary (where N_b is the total number of primordial binaries). The secondary masses are drawn from a distribution that is uniform in the mass ratio within the range $0.1\,M_\odot - m_\mathrm{p}$, where m_p is the primary star mass. The semi-major axes of the binaries are chosen from a distribution flat in $\log a$, where the hardest binary has $a > 5 \times (R_1 + R_2)$, where R_1 and R_2 are the radii of the binary components, and the softest binary is within the local hard-soft boundary (i.e., all primordial binaries are initially hard). The binary eccentricities are chosen from the thermal distribution (e.g., Heggie & Hut 2003).

We vary the initial number of stars ($N = 2 \times 10^5$, 8×10^5, and 1.6×10^6), the initial King concentration parameter ($W_\mathrm{o} = 2$, 5, 7) and the Galactocentric distance R_G, which in our models corresponds to three different metallicities ($Z = 0.005$ at $R_\mathrm{G} = 2$ kpc, $Z = 0.001$ at $R_\mathrm{G} = 8$ kpc and $Z = 0.0001$ at $R_\mathrm{G} = 20$ kpc). The choice to vary metallicity as a function of R_G was motivated by the observations of the Milky Way GC population, which show a correlation between R_G and Z, with larger metallicities being found closer to the Galactic center (Djorgovski & Meylan 1994). These initial conditions form a $3 \times 3 \times 3$ grid of 27 cluster models. Each of these models has initial virial radius $R_\mathrm{v} = 2$ pc and binary fraction $f_\mathrm{b} = 10\%$. We will call these 27 models our *standard models*, and name them according to the values of the three parameters N, W_o, and R_G (e.g. `n8w5rg20` has $N = 8 \times 10^5$, $W_\mathrm{o} = 5$, and $R_\mathrm{G} = 20$ kpc, with metallicity $Z = 0.0005$ set by R_G).

Table 1. Initial model parameters.

model	N (10^5)	M ($10^5 M_\odot$)	W_0	$R_{\rm v}$ pc	$R_{\rm G}$ (kpc)	Z	$f_{\rm b}$ %	$r_{\rm c,dyn}$ (pc)	$r_{\rm h,m}$ (pc)	$\log_{10}(\rho_{\rm c})$ ($M_\odot/{\rm pc}^3$)
n2w2rg2	2	1.36	2	2	2	0.005	10	1.0	1.7	4.47
n2w2rg8	2	1.36	2	2	8	0.001	10	1.0	1.7	4.47
n2w2rg20	2	1.36	2	2	20	0.0005	10	1.0	1.7	4.47
n2w5rg2	2	1.36	5	2	2	0.005	10	0.7	1.6	4.75
n2w5rg8 †	2	1.36	5	2	8	0.001	10	0.7	1.6	4.75
n2w5rg20	2	1.36	5	2	20	0.0005	10	0.7	1.6	4.75
n2w7rg2	2	1.36	7	2	2	0.005	10	0.4	1.6	5.25
n2w7rg8	2	1.36	7	2	8	0.001	10	0.4	1.6	5.25
n2w7rg20	2	1.36	7	2	20	0.0005	10	0.4	1.6	5.25
n2-A	2	1.36	11	2	8	0.001	10	0.1	2.0	7.44
n2-B †	2	1.36	5	1	8	0.001	10	0.4	0.8	5.65
n2-C	2	1.36	5	4	8	0.001	10	1.4	3.3	3.85
n2-D	2	1.29	5	2	8	0.001	1	0.7	1.6	4.71
n2-E	2	1.66	5	2	8	0.001	50	0.7	1.6	4.83
n8w2rg2	8	5.4	2	2	2	0.005	10	1.0	1.7	5.13
n8w2rg8	8	5.4	2	2	8	0.001	10	1.0	1.7	5.13
n8w2rg20	8	5.4	2	2	20	0.0005	10	1.0	1.7	5.13
n8w5rg2	8	5.4	5	2	2	0.005	10	0.7	1.6	5.43
n8w5rg8 †	8	5.4	5	2	8	0.001	10	0.7	1.6	5.43
n8w5rg20	8	5.4	5	2	20	0.0005	10	0.7	1.6	5.43
n8w7rg2	8	5.4	7	2	2	0.005	10	0.4	1.6	5.94
n8w7rg8	8	5.4	7	2	8	0.001	10	0.4	1.6	5.94
n8w7rg20	8	5.4	7	2	20	0.0005	10	0.4	1.6	5.94
n8-A	8	5.4	11	2	8	0.001	10	0.1	2.0	8.08
n8-B	8	5.4	5	1	8	0.001	10	0.4	0.8	6.34
n8-C	8	5.4	5	4	8	0.001	10	1.4	3.3	4.53
n8-D	8	5.13	5	2	8	0.001	1	0.7	1.6	5.39
n8-E †	8	6.57	5	2	8	0.001	50	0.7	1.6	5.51
n16w2rg2	16	10.82	2	2	2	0.005	10	1.0	1.7	5.38
n16w2rg8	16	10.82	2	2	8	0.001	10	1.0	1.7	5.38
n16w2rg20	16	10.82	2	2	20	0.0005	10	1.0	1.7	5.38
n16w5rg2	16	10.82	5	2	2	0.005	10	0.7	1.6	5.67
n16w5rg8	16	10.82	5	2	8	0.001	10	0.7	1.6	5.67
n16w5rg20	16	10.82	5	2	20	0.0005	10	0.7	1.6	5.67
n16w7rg2 †	16	10.82	7	2	2	0.005	10	0.5	1.6	6.18
n16w7rg8	16	10.82	7	2	8	0.001	10	0.5	1.6	6.18
n16w7rg20 †	16	10.82	7	2	20	0.0005	10	0.5	1.6	6.18
n16-A	16	10.82	11	2	8	0.001	10	0.1	2.0	8.32
n16-B	16	10.82	5	1	8	0.001	10	0.4	0.8	6.58
n16-C	16	10.82	5	4	8	0.001	10	1.4	3.3	4.77
n16-D	16	10.28	5	2	8	0.001	1	0.7	1.6	5.65
n16-E	16	13.19	5	2	8	0.001	50	0.7	1.6	5.77

Note. — Initial conditions for all 42 models. Columns are as follows: model name, number of stars (N), total cluster mass (M) in $M_\odot$, King concentration parameter ($W_{\rm o}$), virial radius ($R_{\rm v}$) in pc, galactocentric distance ($R_{\rm G}$) in kpc, metallicity (Z), binary fraction (%), theoretical (mass-density weighted) core radius ($r_{\rm c,dyn}$) in pc (Casertano & Hut 1985), theoretical half mass radius ($r_{\rm h,m}$) in pc, initial central 3D mass density in ($\log_{10}(\rho_{\rm c})$) in $M_\odot/{\rm pc}^3$. The six models with a dagger by their name indicate the representative models that we have chosen to illustrate in several of the figures.

We have also run fifteen additional models in which we have either extended the range of one of the parameters varied in the standard models, or varied a new parameter. For each N, starting with our intermediate parameters ($W_o = 5$, R_G=8 kpc, Z=0.001), we have created models with larger central concentration ($W_o = 11$), with smaller and larger initial binary fraction ($f_b = 1\%$ and 50%), and with smaller and larger virial radius ($R_v = 1$, 4 pc). At a given N, these models are designated with the letters A through E (e.g., `n2-A`) representing $W_o = 11$ (A), $R_v = 1$ pc (B), $R_v = 4$ pc (C), $f_b = 1\%$ (D) and $f_b = 50\%$ (E). Rather than attempting to reproduce the distribution of cluster properties observed in the MW GCs, our goal is to see whether GCs with many BHs can evolve into ~ 10 Gyr old clusters that are consistent with the properties of MW GCs. We evolve all of our models to a final time[1] of 12 Gyr, which is a typical age for MW GCs. The properties of our initial models are given in Table 1.

For typical IMFs (e.g., Kroupa), a fraction of $\sim 10^{-4} - 10^{-3}\,N$ stars should become BHs, depending on the exact mass range assumed for the IMF and the details of the stellar evolution assumptions (e.g., the metallicity-dependent separation between NS and BH progenitors). For our low-, intermediate- and large-N models, we form produce around 450, 1750, and 3500 BHs, respectively, which form from stars with initial masses above about $19\,M_\odot$. The BH mass spectrum depends significantly on the metallicity assumed. In the Belczynski et al. (2002) remnant prescription used here the BH masses range from $\sim 3 - 30\,M_\odot$ for $Z = 0.0005$ and $Z = 0.001$, but at higher metallicities ($Z = 0.005$ here), mass loss from stronger stellar winds causes the upper end of the BH mass function to be truncated at about 20 $M_\odot$. For $Z = 0.001$, about 36% of the BHs are formed through partial fallback, and only these BHs receive natal kicks. The rest of the BHs are formed through direct collapse.

4. Results

4.1. Typical Evolution of Clusters with Black Holes

We start by describing the qualitative evolution common to all of our cluster models, and in later sections we describe in more detail the properties of the retained and ejected BH populations, as well as observable cluster properties. In what follows, whenever it is reasonable to show the results for all of our models we do so, but for cases when this is not possible, we have chosen three pairs of models (each with different N) that are identical except for one parameter, to allow us to see the effect that the virial radius, the binary fraction, and the Galactocentric distance together with metallicity, have on our results. The pairs of models we selected are `n2w5rg8` and `n2-B` ($R_v = 2$ pc and $R_v = 1$ pc), `n8w5rg8` and `n8-E` ($f_b = 10\%$ and $f_b = 50\%$), and `n16w7rg2` and `n16w7rg20` ($R_G = 2$ kpc with $Z = 0.005$ and $R_G = 20$ kpc with $Z = 0.0005$).

[1]Three of our low-N models evaporated before 12 Gyr, ending the simulation early.

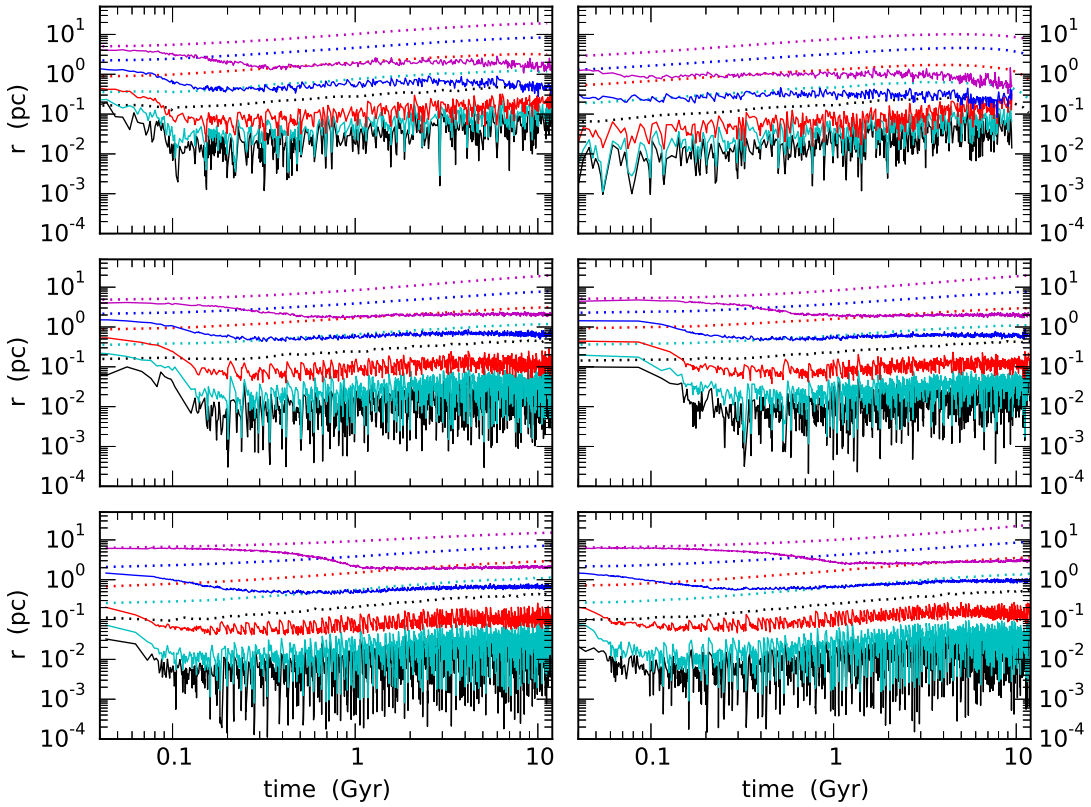

Fig. 2.— Evolution of the Lagrange radii for a subset of models, calculated separately for the BHs (solid curves) and for all other objects (dotted curves). The six models shown are as follows: *top left*: `n2w5rg8`; *top right*: `n2-B`; *center left*: `n8w5rg8`; *center right*: `n8-E`; *lower left*: `n16w7rg2`; *lower right*: `n16w7rg20`. The Lagrange radii shown enclose a fixed fraction of the mass (from bottom to top) of 0.1%, 1%, 10%, 50% and 90%, for each individual component (BHs, non-BHs). The central $\approx 1\%$ BH mass collapses within ≈ 100 Myr, and the rest of the BH mass segregates on a slightly longer timescale, while most of the rest of the cluster steadily expands. After a few Gyr, the 90% BH Lagrange radius (solid magenta curve) typically crosses inside of the 10% radius for the rest of the cluster (dotted red curve). Model `n2-B` (top right) actually starts to contract near the end.

Most of the BHs form within about 10 Myr and promptly begin to sink due to dynamical friction against the lower-mass background stars. The timescale for segregation of a BH from the half-mass radius to the core is

$$t_{\rm seg} \sim \frac{\langle m \rangle}{m_{\rm BH}} t_{\rm rh} \sim 100\,{\rm Myr} \tag{3}$$

(O'Leary et al. 2006) where $\langle m \rangle$ is the average stellar mass, $m_{\rm BH}$ is the mass of the BH, and $t_{\rm rh} \sim 1$ Gyr is the half-mass relaxation time. Since this timescale is dependent on $m_{\rm BH}$, the most massive BHs tend to sink the fastest, driving a central collapse[2]. This can be seen in Figure 2,

[2]This is different from what is usually referred to as "core collapse," which occurs on a much longer timescale and will be discussed later. Terms such as "core collapse" and "post-collapse" are used inconsistently in the literature, and can mean very different things to different authors, especially theorists vs observers (but the meaning can even vary between theorists) (see Chatterjee et al. 2013).

which shows the Lagrange radii for the six representative models. By looking at the Lagrange radii separately for the BHs (solid lines) and for the non-BHs (dotted lines), we see a clear separation of these two populations, with the BHs becoming more centrally concentrated than the lower-mass stars. A small subset (about 1%) of the BH mass goes through radial oscillations where the 1% Lagrange radius can vary by as much as two orders of magnitude. The other 99% of the BH mass remains confined to roughly the same region for all time as the rest of the cluster slowly expands. The 90% BH Lagrange radius is typically at about $1 - 2$ pc, and coincides roughly with the 10% Lagrange radius for the other (non-BH) stars.

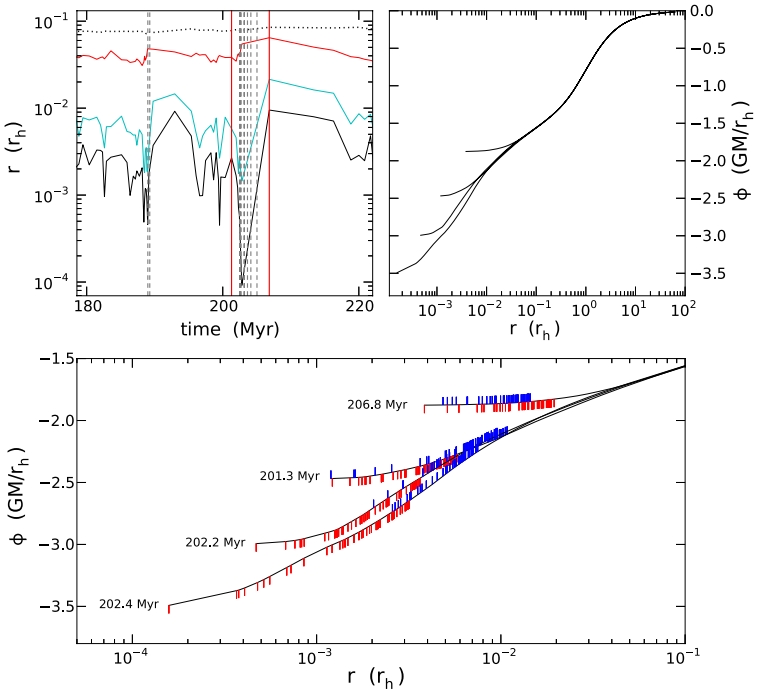

Fig. 3.— Time variation of central gravitational potential through a core oscillation around 200 Myr for model `n16w7rg20` (lower right panel in Figure 2). *Top left*: zoom-in on the Lagrange radii from about 180–220 Myr. The radial coordinate is given in units of the initial half-mass radius ($r_{\rm h}(0)$). The three solid curves are the 0.1%, 1% and 10% (*from bottom to top*) Lagrange radii of the BHs, and the dotted curve is the 0.1% radius for all non-BH stars. The vertical dashed lines indicate the times when three-body binaries were formed. The vertical solid red lines specify the period of time that we focus on in both the right and the lower panels, which covers a deep collapse and subsequent re-expansion. *Top right*: the full gravitational potential, $\phi(r)$, at four different times (as indicated on the lower panel), in units of $G\,M/r_{\rm h}$, where M is the total cluster mass and $r_{\rm h}$ is the half-mass radius, at that particular time. *Bottom*: zoom-in on the central potential, showing the radial positions of the innermost 50 BHs (*red ticks*) and non-BHs (*blue ticks*) at each time.

In Figure 3 we zoom-in on one of the core oscillations for model `n16w7rg20` (lower right panel of Figure 2) to show how the cluster potential fluctuates over a timescale of just a few Myr. During the collapse of the innermost 1% BH mass, the BHs segregate from the lower-mass stars, forming a *short-lived* cusp of mostly BHs. In the deepest part of the collapse, the central ≈ 30 objects are *all* BHs. Several three-body binaries form during this phase (see top left panel) and their interactions with other objects ultimately power the re-expansion, after which the 1% BH radius is even larger than it was pre-collapse. At this point the BHs have become mixed with the other

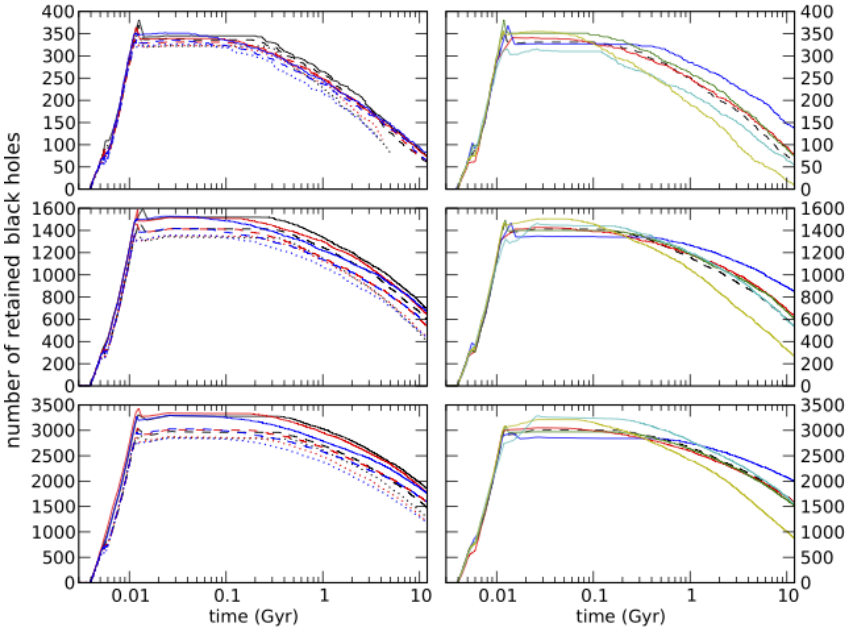

Fig. 4.— Evolution of total number of retained BHs for all models. From top to bottom, the adjacent panels show all models with initial $N = 2 \times 10^5$, $N = 8 \times 10^5$, $N = 1.6 \times 10^6$. On the left we show the nine standard models at each N. The color indicates the initial central concentration ($W_o = 2$ in black, $W_o = 5$ in red, and $W_o = 7$ in blue), the linestyle indicates the initial galactocentric distance and metallicity (solid lines for $R_G = 20$ kpc and $Z = 0.0005$, dashed lines for $R_G = 8$ kpc and $Z = 0.001$, and dotted lines for $R_G = 2$ kpc and $Z = 0.005$. All models on the left have $R_v = 2$ pc and $f_b = 10\%$. On the right we show the five additional models at each N, along with the standard model for that N with intermediate parameters (i.e., $W_o = 5$, $R_G = 20$ kpc, $Z = 0.0005$, $R_v = 2$ pc, $f_b = 10\%$) for comparison (black dashed curve). Each of the solid colored lines has one parameter slightly different from this intermediate model, as follows: $W_o = 11$ shown in red, $R_v = 1$ pc and 4 pc in yellow and blue, respectively, and $f_b = 1\%$ and 50% in green and cyan, respectively. The three models on the top left that end before reaching 12 Gyr (dotted lines) are clusters at $R_G = 2$ kpc that evaporated.

stars once again. These core oscillations occur frequently, anywhere from $\sim 10 - 100$ times over 12 Gyr, depending on the model (see Figure 2). The frequency and depth of the oscillations both depend on N (i.e., deeper and more frequent for larger N). The oscillations also tend decrease in frequency and become more shallow over time. Following the initial phase of BH segregation and rapid ejection (up to about a Gyr), the number of oscillations per Gyr decreases from as many as a few tens per Gyr (from 1–2 Gyr) down to just a few per Gyr near the end.

We show the evolution of the total number of BHs present in each model in Figure 4. We see most of the BHs forming up to about 10 Myr, as expected, and then after about 100 Myr, once the most massive BHs have segregated, the number of BHs starts to decrease as they are ejected through strong binary encounters in the core. The number of BHs continues to decrease all the way to 12 Gyr, but the rate slows down over time. The majority of our low-, intermediate-, and large-N models end with roughly 50–100 BHs, 400–800 BHs, and 1000–2000 BHs, respectively. While larger-N models have more BHs at 12 Gyr than lower-N models, they also eject a greater number of BHs in total.

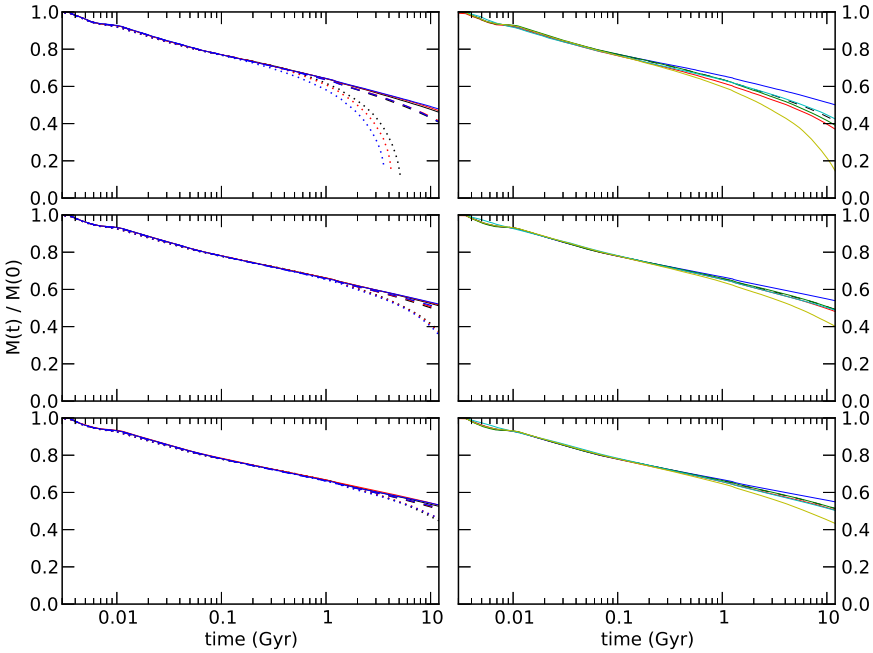

Fig. 5.— Evolution of the total cluster mass for all models. The various curves are described in Figure 4. Nearly all models lose about half of their mass over 12 Gyr. Models with smaller $R_{\rm G}$ (dotted lines on left panels) lose mass at a faster rate, and the smallest of these models actually evaporate prior to 12 Gyr (top left panel). On the right panels, the virial radius has the greatest impact on mass loss, with the models having the smallest initial virial radii (yellow curves) losing mass at a faster rate than the rest, which is most evident for $N = 2 \times 10^5$ (top right).

Figure 5 shows the evolution of total cluster mass for all models. After a period of rapid mass loss driven by early stellar evolution of massive stars, the cluster mass loss rate tends to slow continually over time. Most of our models lose about half of their mass by 12 Gyr, but the most compact clusters (with initial $R_{\rm v} = 1\,{\rm pc}$) and those at the smallest Galactocentric distances ($R_{\rm G} = 2$ kpc), which have the smallest tidal radii, lose mass at faster rates. In fact, among our low-N models, the three with $R_{\rm G} = 2$ kpc (`n2w5rg2, n2w5rg2, n2w7rg2`) nearly completely evaporate within about 6 Gyr (dotted lines in the upper left panel of Figure 5), and the model with $R_{\rm v} = 1$ pc (`n2-B`) has lost more than 80% of its mass by the end of the simulation. The mass loss rate does not change significantly over the range $R_{\rm G} = 8 - 20$ kpc. The final structural properties for all of our models are shown in Table 2. Note that these are all *theoretical* properties (e.g., the density and core radius are computing using all objects, not just luminous stars that can actually be observed). Observable properties of our clusters are discussed later.

4.2. Retained Black Hole Populations

Next we look at the properties and evolution of the retained BHs in more detail and discuss differences among our models. The initial BH mass spectrum is shown in Figure 7, and aside from

Table 2. Final cluster properties.

model	N (10^5)	M ($10^5 M_\odot$)	$r_{\rm c,dyn}$ (pc)	$r_{\rm h,m}$ (pc)	$\log_{10}(\rho_{\rm c})$ ($M_\odot/{\rm pc}^3$)	f_b %	$f_{\rm b,core}$ %
n2w2rg2	0.04	0.03	0.0	2.6	6.2	15.5	16.7
n2w2rg8	1.43	0.55	2.9	7.8	2.64	9.5	12.0
n2w2rg20	1.65	0.63	3.2	8.6	2.54	9.3	11.8
n2w5rg2	0.02	0.03	0.4	1.6	3.84	13.0	6.0
n2w5rg8 †	1.46	0.56	3.1	8.3	2.95	9.5	12.3
n2w5rg20	1.68	0.64	3.1	8.9	3.08	9.3	11.3
n2w7rg2	0.03	0.03	0.3	2.0	4.71	13.2	6.3
n2w7rg8	1.44	0.56	3.5	8.9	2.74	9.5	12.3
n2w7rg20	1.72	0.65	3.7	9.8	2.54	9.3	12.0
n2-A	1.28	0.5	3.8	9.4	2.69	9.5	11.4
n2-B †	0.37	0.2	0.5	2.9	4.76	12.3	25.8
n2-C	1.79	0.68	6.0	13.3	1.88	9.4	10.9
n2-D	1.36	0.51	3.6	8.6	2.37	1.0	1.0
n2-E	1.54	0.71	2.7	7.7	3.31	46.5	53.7
n8w2rg2	5.12	2.04	2.5	6.2	3.91	9.3	10.9
n8w2rg8	6.86	2.62	2.2	7.9	5.23	9.1	10.2
n8w2rg20	7.25	2.76	3.3	8.5	3.61	9.0	9.7
n8w5rg2	4.99	2.0	2.7	6.6	3.69	9.4	10.7
n8w5rg8 †	7.0	2.66	3.2	7.9	3.42	9.1	10.1
n8w5rg20	7.36	2.79	3.2	8.6	3.80	9.4	10.0
n8w7rg2	4.77	1.92	2.8	6.9	4.03	9.4	11.1
n8w7rg8	7.11	2.7	3.4	8.6	3.45	9.1	10.0
n8w7rg20	7.41	2.81	0.0	9.3	8.98	9.0	4.8
n8-A	6.77	2.6	2.8	9.0	4.74	9.1	9.7
n8-B	5.56	2.17	1.7	4.9	4.28	9.1	11.9
n8-C	7.6	2.91	3.9	11.7	4.44	9.2	9.7
n8-D	6.87	2.52	3.0	8.3	4.29	1.0	1.0
n8-E †	7.19	3.21	2.9	7.7	3.93	45.1	47.5
n16w2rg2	12.38	4.84	1.4	6.4	6.47	9.1	10.0
n16w2rg8	14.39	5.5	1.6	7.5	6.16	8.9	9.3
n16w2rg20	14.82	5.68	3.0	8.0	4.32	8.9	9.2
n16w5rg2	12.77	4.97	2.1	6.6	5.34	9.1	10.1
n16w5rg8	14.54	5.56	2.4	7.8	5.42	9.0	9.5
n16w5rg20	14.82	5.76	0.0	8.5	10.1	8.9	25.0
n16w7rg2 †	12.79	4.96	2.9	7.1	4.08	9.1	10.0
n16w7rg8	14.61	5.58	2.8	8.4	4.98	9.0	9.3
n16w7rg20 †	15.11	5.76	2.9	8.8	4.69	8.9	9.0
n16-A	14.23	5.47	3.3	8.5	3.93	8.9	9.2
n16-B	12.17	4.69	1.5	5.1	5.85	9.0	10.5
n16-C	15.46	5.94	4.8	11.1	3.67	9.1	9.4
n16-D	14.38	5.28	2.9	7.8	4.48	1.0	0.9
n16-E	14.8	6.63	3.0	7.6	4.04	44.7	45.0

Note. — Columns are as follows: model name, number of stars (N), total mass (M) in $M_\odot$, theoretical (mass-density weighted) core radius ($r_{\rm c,dyn}$) in pc (which is very different from that which an observer would measure; see Section 4.5 and Table 4), half-mass radius ($r_{\rm h,m}$) in pc, central 3D mass density in ($\log_{10}(\rho_{\rm c})$) in $M_\odot/{\rm pc}^3$, final overall binary fraction ($f_{\rm b}$), and final binary fraction in the core ($f_{\rm b,core}$), as defined above. All properties are calculated at $t = 12$ Gyr, except for models `n2w2rg2`, `n2w5rg2` and `n2w7rg2`, which evaporated prior to 12 Gyr. For these models, the properties are calculated at the time when we deemed the cluster to have almost completely evaporated (when there are only about 1000 stars remaining), which happens at 5.2, 4.2, and 3.6 Gyr respectively for the models listed above. As in Table 1, the six representative models shown in several of the figures are marked with a dagger. A core size of 0.0 (`n2w2rg2`, `n8w7rg20`, `n16w5rg20`) means that the BH core is in a collapsed state at the end of the simulation, so the core is extremely small and ill-defined. This is of course unrelated to the core radius that an observer would calculate. The exceptionally small and large final core binary fractions in models `n8w7rg20` and `n16w5rg20` (respectively) has to do with their being in a collapsed state, where the core is composed of a very small number of stars, and thus the binary fraction is quite sensitive to small fluctuations in the core composition.

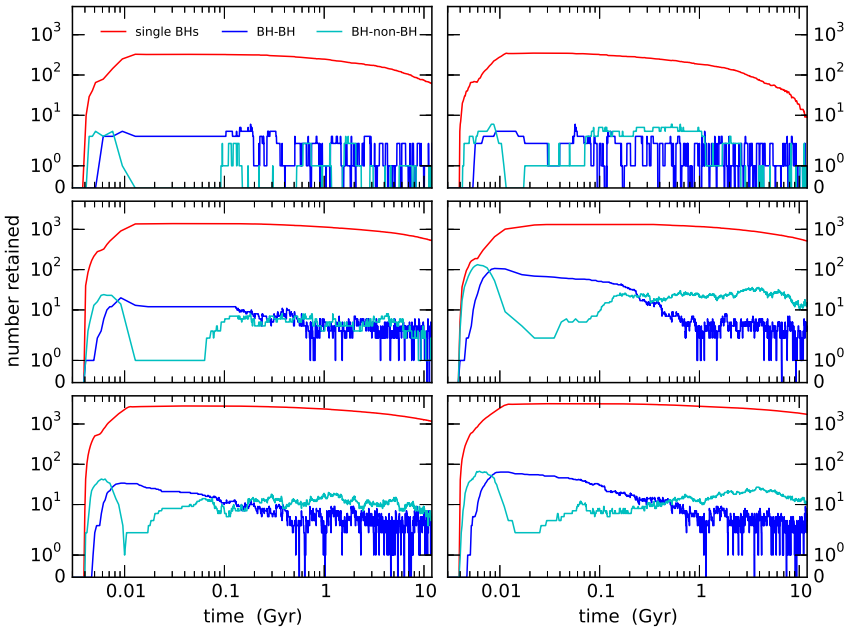

Fig. 6.— Numbers of *retained* single and binary BHs as a function of time for the six models shown in Figure 2. Numbers of single BHs are in red, BH–BH binaries in blue, and BH–non-BH binaries in cyan. Nearly all retained BHs are single. With increasing N (top to bottom) the number of BHs in binaries increases slightly. A larger binary fraction (center right, $f_{\rm b} = 50\%$, compared to 10% on left) allows more BHs to be in binaries (mostly BH–non-BH), but does not have a significant impact on overall BH retention. The number of BH binaries is not affected significantly by either virial radius (compare top panels) or $R_{\rm G}$ and Z (compare lower panels).

the normalization, the only factor that significantly affects the mass function is the metallicity Z. Since massive and metal-rich stars lose more mass via stellar winds, they form less massive BHs than do lower metallicity stars (see lower right panel). Our models retain between $65 - 90\%$ of the BHs *initially*, depending primarily on $R_{\rm G}$ (and Z) and $R_{\rm v}$. The reason for the $R_{\rm G}$ and Z dependence of the initial retention fraction is twofold: First, a BH with a given position and kick speed will escape more easily from the cluster with the smaller tidal radius. Additionally, since models with smaller $R_{\rm G}$ also have larger Z, the BHs produced have lower masses and will therefore tend to receive stronger kicks, making these objects even more likely to be ejected upon formation. More compact clusters (small $R_{\rm v}$) can retain initially formed BHs more easily.

In Figure 6 we show the distribution of single and binary BHs as a function of time for our six representative models. Here we see that almost all of the retained BHs remain as single stars throughout the cluster evolution, in agreement with our earlier results (Morscher et al. 2013). There are usually no more than a few tens of BH binaries of any type inside the clusters at any given time, and are usually made up of comparable numbers of BH–BH and BH–non-BH binaries. A larger supply of primordial binaries does provide more opportunities for BHs to exchange into binaries through dynamical interactions and so we see a slightly larger number of BH binaries in models with larger $f_{\rm b}$. This effect can be seen in the center panels in Figure 6, where we compare model

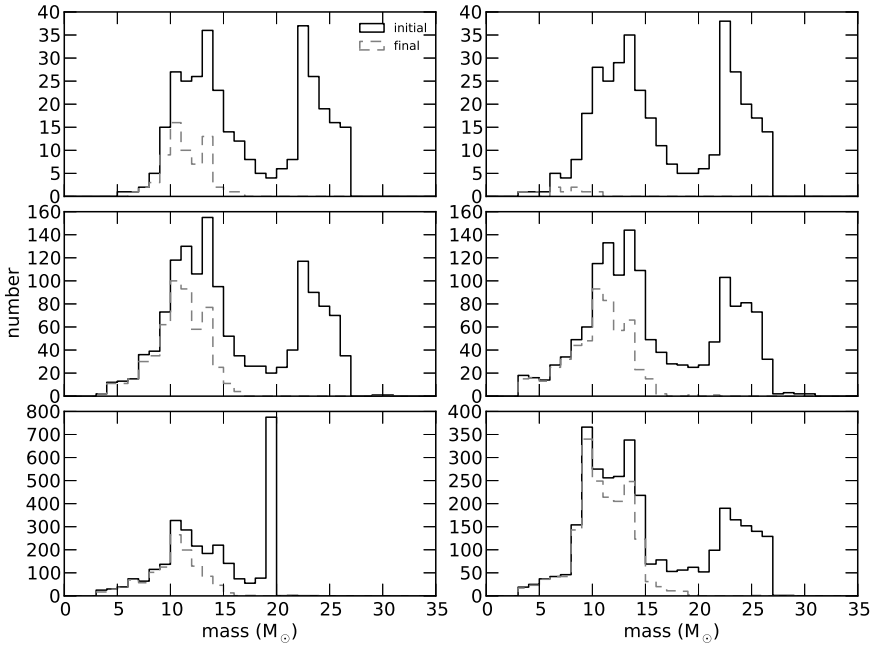

Fig. 7.— BH mass spectrum initially (i.e., at a time between $30 - 100$ Myr) (solid black lines) and at 12 Gyr (dashed grey lines) for the same six models described in Figure 2. The 'initial' BH mass spectrum is based on the BHs in the cluster at an early time (around 30-100 Myr, depending on model). The most massive BHs are always the first to be ejected, which reduces the initially double-peaked BH mass spectrum to a single peak. The maximum BH mass and location of the peak depends on the fraction of BHs that have been ejected. The initial BH mass spectrum looks very different for high Z (compare lower panels, with $R_{\rm G} = 2$ kpc and $Z = 0.005$ on the left and $R_{\rm G} = 20$ kpc and $Z = 0.0005$ on the right; note that the different y-axis scales are different). For large Z, mass lost from stellar wind (most significant for massive stars) prevents the most massive BHs (above $20\,M_\odot$) from forming, and causes the pileup of BHs at about $20\,M_\odot$, which results from a flattening of the progenitor-to-remnant mass relation (see Figure 1 of Belczynski et al. 2004). Model `n2-B` (top right) has $R_{\rm v} = 1$ pc and ejects nearly all of its BHs, leaving behind just 9 BHs with masses of $3 - 10\,M_\odot$.

`n8-E` ($f_{\rm b} = 50\%$, right) to model `n8w5rg8` ($f_{\rm b} = 10\%$, left). Since most of the primordial binary population consists of two low-mass stars initially (which will never become BHs), the number of BH–non-BH binaries is most affected by the primordial binary fraction. The other parameters seem to have only a minor effect on the number of BH binaries in clusters.

The final retained BH mass distributions are shown in Figure 7 along with the initially retained population, for comparison. Since the most massive BHs segregate the deepest they also interact the most frequently, and therefore tend to be the first to be ejected. Over time, the maximum BH mass in the cluster is reduced from about $25-30\,M_\odot$ initially down to about $15-20\,M_\odot$ at 12 Gyr. Many of our models still contain a substantial population of $\approx 10\,M_\odot$ BHs at 12 Gyr. The fraction of (initially retained) BHs that are retained all the way to 12 Gyr depends strongly on N. For our largest-N clusters, the final retention fraction $f_{\rm BH,12}$ is typically about 50%, and for the lowest-N clusters $f_{\rm BH,12}$ is only about 20% (except for the special case of model `n2-B`, which we will discuss separately). Since the initial number of BHs *and* the final BH retention fraction both scale with N, the final *number* of BHs grows faster than linearly with N. The final properties of the populations

of retained and ejected BHs for each model are given in Table 3.

Looking back to Figure 4 we see that models with smaller $R_{\rm G}$ retain fewer BHs at 12 Gyr, but this is primarily because they retained fewer BHs *initially*. Although larger primordial binary fractions produce a slightly larger number of BHs in binaries, this has little impact on the final number of retained BHs. For example, comparing models with $N = 1.6 \times 10^6$ and $f_{\rm b} = 1\%$ and 50% (`n16-D` and `n16-E`), the final number of retained BHs at 12 Gyr is 1512 and 1556, respectively (see Table 3 for details). Rather, it seems that three-body binaries play a much more significant role in overall BH evaporation (although, as we will show later, the binary fraction does impact the number of ejected BH–non-BH binaries, as well as the number of in-cluster BH–BH mergers). By far, the initial virial radius has the greatest impact on the BH evaporation rate for models with a given N. More compact clusters with smaller $R_{\rm v}$ are more dense, and so they process their BHs at a faster rate and therefore end with significantly fewer BHs (compare the yellow and blue curves on each panel on the right hand side of Figure 4). Furthermore, since the massive BHs are depleted to a greater extent, the remaining population is composed of BHs with comparatively low masses. The model with the fewest BHs remaining at 12 Gyr is `n2-B`, our low-N model with $R_{\rm v} = 1$ pc, which has just 9 BHs at 12 Gyr, or $f_{\rm BH,12}$= 2% (compared to 135 BHs for model `n2-C` with $R_{\rm v} = 4$ pc, but same initial conditions otherwise). We see a similar trend in BH retention in our more massive cluster models, but the contrast is not quite as stark (269 BHs retained in model `n8-B` compared to 852 in model `n8-C`; 869 BHs retained in model `n16-B` compared to 1988 in model `n16-C`). It seems that the only way to get rid of most or all of the BHs is to start with very small $R_{\rm v}$.

4.3. Ejected Black Hole Binaries

We now examine the ejected BH populations with a focus on BH binaries. In Figure 8 we show the cumulative number of binary-binary (B-B) and binary-single (B-S) interactions along with the total number of ejected single BHs, BH–BH binaries, and BH–non-BH binaries as a function of time. The early phase of rapid BH ejection is associated with BHs that are ejected at birth via supernova kicks prior to 10 Myr, and is followed by a flattening of the BH ejection rate, during which time the BHs are segregating. Once the BHs have segregated sufficiently, the dynamical BH ejections begin, typically by about $100 - 300$ Myr. In more massive clusters with higher central densities, binary interactions begin much more gradually, but also earlier, so they have already become important well before the BHs have formed. In the lower-N models, binary interactions begin later, and in some cases the segregation of BHs actually drives an increase in the rate of binary interactions (e.g., top left and center left panels in Figure 8). As in the case of the retained BHs, the ejected BHs too are mostly single. In order to eject a BH binary, it typically has to participate in multiple binary interactions in order to harden enough that the recoil from some final interaction is sufficient to remove it from the cluster entirely. The binaries that are ejected, therefore, are most often BH–BH binaries, since through many strong interactions, any low-mass

Table 3. Numbers of BHs retained in and ejected from each cluster.

model	initial formed/ret	final retained total	single	BH–BH	BH-WD	BH-star	final ejected total	single	BH–BH	BH-WD	BH-star	mergers ret / ej
n2w2rg2	430 / 322	81	76	2	0	1	312	245	33	0	1	0 / 9
n2w2rg8	459 / 336	58	57	0	0	1	381	304	36	0	5	0 / 5
n2w2rg20	474 / 345	76	74	1	0	0	384	291	45	0	3	1 / 4
n2w5rg2	427 / 323	111	110	0	0	1	285	232	25	0	2	0 / 6
n2w5rg8 †	457 / 331	65	61	2	0	0	361	287	36	0	2	0 / 6
n2w5rg20	471 / 339	73	71	1	0	0	393	298	44	0	7	0 / 12
n2w7rg2	433 / 326	116	111	2	0	1	297	237	29	0	2	0 / 5
n2w7rg8	459 / 330	66	62	2	0	0	369	302	31	0	5	0 / 6
n2w7rg20	477 / 347	82	77	2	0	1	378	302	35	0	6	2 / 5
n2-A	464 / 338	76	72	1	1	1	368	290	37	0	4	0 / 4
n2-B †	463 / 350	9	9	0	0	0	428	317	54	0	3	1 / 12
n2-C	454 / 327	135	128	3	0	1	309	251	25	0	7	1 / 1
n2-D	456 / 351	74	70	2	0	0	362	290	36	0	0	0 / 1
n2-E	472 / 310	55	51	1	0	2	386	286	41	0	18	8 / 18
n8w2rg2	1689 / 1338	399	391	2	0	4	1181	923	127	0	3	8 / 58
n8w2rg8	1788 / 1413	598	586	3	1	5	1120	917	101	0	1	14 / 52
n8w2rg20	1813 / 1519	690	680	4	0	2	1056	822	116	0	2	14 / 57
n8w5rg2	1692 / 1349	429	422	1	0	5	1163	920	120	0	2	8 / 67
n8w5rg8 †	1779 / 1412	533	525	3	0	2	1182	926	127	0	2	12 / 65
n8w5rg20	1809 / 1512	643	634	4	0	1	1112	860	122	0	6	15 / 57
n8w7rg2	1698 / 1355	437	426	3	0	5	1154	891	130	1	2	5 / 69
n8w7rg8	1780 / 1417	562	553	4	0	1	1149	907	120	0	1	14 / 68
n8w7rg20	1815 / 1520	666	659	1	0	5	1109	837	133	0	6	17 / 68
n8-A	1790 / 1419	638	623	4	2	5	1098	874	105	1	10	0 / 57
n8-B	1809 / 1503	269	263	1	1	3	1461	1112	174	0	1	9 / 115
n8-C	1747 / 1346	852	837	4	2	5	857	708	68	0	10	11 / 25
n8-D	1749 / 1401	602	594	4	0	0	1104	901	101	0	1	0 / 51
n8-E †	1949 / 1446	534	514	3	0	14	1262	922	157	0	24	56 / 97
n16w2rg2	3477 / 2850	1261	1250	2	0	7	2050	1608	220	0	2	25 / 181
n16w2rg8	3634 / 2966	1473	1464	2	0	5	2048	1618	213	0	4	30 / 159
n16w2rg20	3737 / 3282	1848	1831	4	1	8	1801	1358	219	0	5	20 / 179
n16w5rg2	3458 / 2864	1202	1194	0	0	8	2099	1613	242	0	2	20 / 194
n16w5rg8	3659 / 3008	1585	1566	5	1	8	1974	1563	204	0	3	27 / 152
n16w5rg20	3841 / 3333	1770	1748	5	1	11	1951	1453	244	0	8	21 / 194
n16w7rg2 †	3447 / 2844	1176	1163	4	0	5	2078	1628	222	0	6	17 / 180
n16w7rg8	3638 / 3026	1587	1570	4	2	7	1949	1545	198	0	7	15 / 159
n16w7rg20 †	3721 / 3283	1757	1738	4	0	11	1867	1407	225	0	8	31 / 168
n16-A	3666 / 3043	1582	1559	7	0	9	2012	1606	197	0	7	0 / 156
n16-B	3703 / 3213	869	859	2	1	5	2710	2027	337	0	4	21 / 287
n16-C	3610 / 2852	1988	1967	4	1	12	1536	1242	145	0	3	30 / 98
n16-D	3548 / 2972	1512	1502	5	0	0	1954	1576	189	0	0	3 / 142
n16-E	4259 / 3250	1556	1497	5	4	45	2330	1771	269	1	17	156 / 235

Note. — The first two columns are the model name and the total number of BHs that formed/retained initially in each model; columns 3–7 give the total number of BHs, single BHs, BH–BH, BH–WD, and BH–star binaries *retained* through the end of each simulation; similarly columns 8–12 give the total number of BHs, single BHs, BH–BH, BH–WD, and BH–star binaries *ejected* by the end of each simulation. The final column shows the number of mergers that occur within the cluster/post ejection from the cluster.

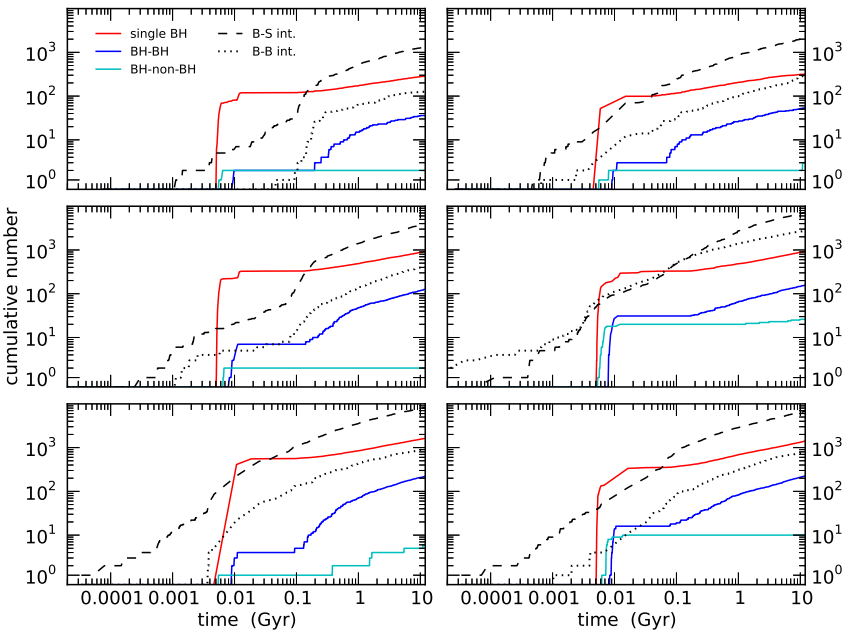

Fig. 8.— Cumulative number of binary interactions and ejected BHs as a function of time for the six models shown in Figure 2. Black dashed and dotted curves show the cumulative number of binary-binary (B-B) and binary-single (B-S) interactions, respectively. The solid curves show the cumulative number of ejected single BHs (red), BH–BH binaries (blue), and BH–non-BH binaries (cyan). The sharp increase at around 10 Myr shows BHs that are ejected via natal kicks. In many models, we see an increase in the binary interaction rate after about 100 Myr, and an associated increase in the BH–BH ejection rate. Most of the ejected BH binaries are BH–BH binaries. Models with binary fraction $f_{\rm b} = 50\%$ (center right) have similar B-S and B-B interaction rates, while all other models with lower binary fractions have many more single stars than binaries, and hence have mostly B-S interactions.

non-BH binary companions will be preferentially replaced by BHs. This holds true even though there are usually about as many (and sometimes more) BH–non-BH binaries present in our models as there are BH–BH binaries.

We find that most of the (small number of) BH–non-BH binary ejections happen early, at the time of formation of the BH, rather than through subsequent dynamics. Most models have many more B-S interactions than B-B interactions, since with $f_{\rm b} = 10\%$ there are many more single stars than binaries, but with $f_{\rm b} = 50\%$, there are about equal numbers of B-S and B-B interactions. In models with large binary fractions (e.g., center right panel in Figure 8), the number of BH–non-BH ejections is greater than in models with fewer binaries, but they still occur primarily at BH formation. There are slightly more dynamical BH–non-BH ejections with higher binary fractions, since there is a greater supply of binaries with which the BHs could interact (the same reason that there are also more BH–non-BH binaries present inside the clusters). In the lower panels in Figure 8 we see that in the high metallicity cluster (left), fewer BH–non-BH binaries are ejected upon BH formation, and instead are mostly ejected dynamically. This makes sense considering that the the lower-mass BHs produced at high metallicities will receive larger birth kicks, which will unbind (rather than eject) more of these binaries when the BH is formed. Additionally, low-mass

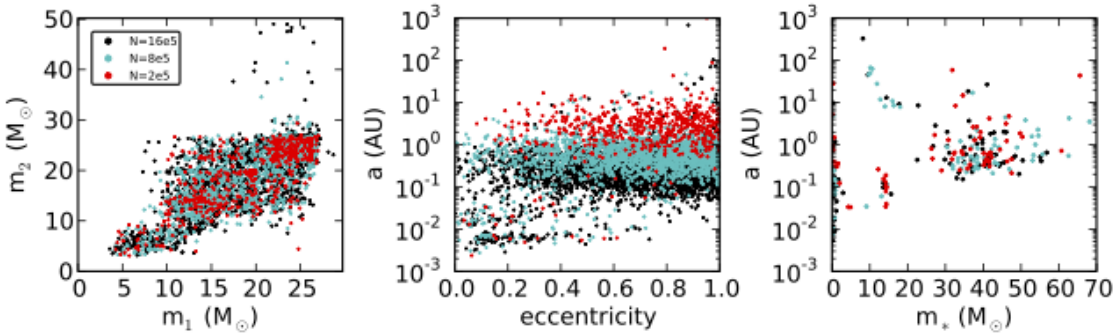

Fig. 9.— Properties of ejected BH binaries at time of ejection from all simulations combined. Each point represents one BH binary, and the color indicates the initial N for the cluster from which the binary originated (black for $N = 1.6 \times 10^6$, cyan for $N = 8 \times 10^5$, and red for for $N = 2 \times 10^5$. The first two panels show properties of the ≈ 5600 ejected BH–BH binaries: on the left, m_2 versus m_1, and in the middle the semi-major axis versus the eccentricity. The masses of the BHs in the ejected BH–BH binaries are similar across all N, while their orbital properties depend strongly on N, with more massive clusters forming and ejecting much tighter BH–BH binaries. On the right we show the semi-major axis and the companion mass for the 227 ejected binaries containing a BH with a non-compact stellar companion. Note that the points are plotted on top of each other (from bottom to top: black, then cyan, then red), so some points are hidden, especially in the left and center panels. The trends are visible, nonetheless.

BHs will also be more likely to interact with normal low-mass stars over time, which explains why this model ejects more BH–non-BH binaries through dynamics than in some other models.

The virial radius has the greatest effect of the ejection rate of BH–BH binaries. The smaller $R_{\rm v}$, the higher the density and therefore also the binary interaction rate. We find that for a given N, models with $R_{\rm v} = 1$ pc eject more than twice the number of BH–BH binaries as models with $R_{\rm v} = 4$. This trend does not hold for ejected BH–non-BH binaries. In fact, for $N = 2 \times 10^5$ and $N = 8 \times 10^5$, the models with smaller virial radii actually eject *fewer* BH–non-BH binaries than those with larger virial radii. Since most of the BH–non-BH binaries are ejected at the time of BH formation rather than through dynamics, we should not expect the rate of these ejections to increase with the higher interaction rates occurring in more compact clusters.

In Figure 9 we show the binary properties for the ejected BH binaries at time of formation, color-coded by the initial N of the model from which it originated. On the first panel we show the masses of the components (m_1 and m_2) of BH–BH binaries ejected from all models. Since all clusters with a given metallicity form the same spectrum of BH masses, and the more massive BHs are ejected before the less massive ones, it is not surprising that the masses of the BHs in ejected BH–BH binaries is nearly independent of N. In the *orbital* properties of ejected BH–BH binaries (center panel), however, we see a very obvious correlation with N. The least massive clusters eject binaries with significantly larger semi-major axes (typically ~ 1 AU) than the most massive clusters (typically ~ 0.1 AU). This follows from the fact that it is easier to eject a binary from a less massive cluster due to its lower escape speed, therefore most of these binaries get ejected before they have a chance to tighten to sub-AU separations. On the right panel we show the semi-major axis and the companion mass for the 227 ejected binaries containing a BH with a non-compact

stellar companion. Recall that most of these binaries are ejected within about 10 Myr, which is why the majority of these systems have massive companions that have not yet evolved into compact objects (note that once ejected, these objects are no longer evolved). There is no obvious trend with N, but there is a weak correlation between a and m_*, with the binaries containing more massive companions tending to have slightly larger separations.

4.4. Merging BHs

The dynamics that leads to BH evaporation also produces very tight BH–BH binaries, many of which merge within the 12 Gyr. These mergers can either occur while the binary is still bound to the cluster or in the field after being ejected. For all of our models combined, we produce 4096 merging systems over the 12 Gyr of evolution. Of these mergers, about 85% occur post-ejection in the field and the other 15% occur inside clusters. Nearly 71% of the mergers are produced in the large-N models, about 26% in the intermediate-N models, and just under 3% in the lowest-N models. The numbers of mergers per model are given in Table 3. The strong N-dependence of the merger rate is caused by two effects. First, we saw that more massive clusters processed more BHs, and therefore ejected a greater number of BH–BH binaries. Also, since more massive clusters tend to eject *tighter* binaries, it turns out that a greater fraction of the ejected binaries actually merge within 12 Gyr. The binary fraction has the next biggest impact of the merger rate, enhancing the rate of post-ejection mergers slightly, but dramatically increasing the rate of in-cluster mergers (going from 1% to 50% binaries, the number of in-cluster mergers for our models increases from 0 to 8, 0 to 56, and 3 to 156, in order of lowest to highest N). This means that it is not only dynamically formed hard three-body binaries that produce BH–BH mergers, but also BH–BH binaries that form and harden through B-B and B-S interactions. Just over 40% of the mergers occur within the first Gyr (about 1700 mergers), and the rate per Gyr decreases dramatically over time, with only about 100 mergers occurring over the last Gyr. If we assume that our models describe the MW GCs reasonably well[3], we can make a very crude estimate of the present-day merger rate by extrapolating to the current total population of about 150 GCs. Multiplying our merger rate (100 Gyr^{-1} during the last Gyr) for $\sim$ 50 models by a factor of 3 (to get 150 clusters) gives us a total merger rate of $\sim$ 0.3 per MWEG per Myr.

This crude estimate agrees with the merger rate that we calculated previously (Morscher et al. 2013), although that rate was averaged over 12 Gyr, which is clearly not reasonable considering how the merger rate decreases over time. Here we use only the mergers that occurred in the last Gyr, making it more appropriate for representing the current merger rate from $\sim$ 10 Gyr old GC systems. This is comparable to the "realistic" merger rate from primordial binaries in galactic fields reported in Abadie et al. (2010), however other more recent studies have predicted both higher (Dominik

[3]But note that our set of models does not cover realistically the parameter space of all MW GCs, as we show in the following section.

et al. 2012) and lower (Mennekens & Vanbeveren 2014) field merger rates. Our estimate is still far too crude to accurately predict the true merger rates from populations of GCs, especially since we see such extreme differences in merger rate across our models. Ideally, the merger rate calculation should factor in how good of a fit our models are to the MW GC population and then weigh the contribution from each model accordingly.

4.5. Observable Properties and Comparison to Galactic GCs

In order to know whether our models are a good representation of reality we must compare observable properties for our models to those of real Galactic GCs. Among these key observable properties are the core radius ($r_{\rm c}$), the ratio of the core radius to the half-light radius ($r_{\rm c}/r_{\rm h}$), the central (3D) luminosity density (ρ_0), and the total cluster mass (M_{cl}). We calculate these four values for each of our models at the final time of 12 Gyr, except for the three models that evaporated prior to 12 Gyr, which are not included in the following analysis.

Since the cluster mass is a straightforward quantity in our models, here we do the simplest thing and report our theoretical total cluster mass, which is the sum of the masses of all the individual stars, including dark remnants. The other three quantities are much more sensitive to the distribution of dark versus luminous stars, and so we must do a bit more work to obtain values that can reasonably be compared to the ones that observers would actually calculate. Since observations of GCs are generally in the V-band, we start by converting the bolometric luminosity for each star as given by BSE to V-band luminosities using the standard stellar library of Lejeune et al. (1998). From there, the half-light radius $r_{\rm h}$ is simply the radius that encloses half of the light (in the V-band). The core radius is a less straightforward quantity, but one that is important for its use in identifying the dynamical state of a GC. There are many different definitions of the core radius, and the resulting values can vary by a factor of a few (Hurley 2007; Trenti et al. 2010). Qualitatively, the core of a cluster is the central region over which the density and velocity dispersion are roughly constant. More quantitatively, the core radius is sometimes defined as the radius at which the surface luminosity density drops to half the central value. To calculate $r_{\rm c}$, observers generally construct a surface brightness profile (SBP), and then measure where the density drops to half the central value. Alternatively, a King model can be fit directly to the SBP. Both of these techniques require radial binning of the stars, which introduces noise (since bright stars are rare) and arbitrariness (choosing a magnitude cutoff to remove brightest stars, choosing the bin size). In order to eliminate the need for binning and to smooth out the noise associated with small numbers of bright stars, we have instead opted to use a new and straightforward approach for calculating $r_{\rm c}$ that uses the *cumulative* luminosity profile. To this we fit the integrated form of a King density profile, and extract the best fit value of $r_{\rm c}$. We find that this function provides an excellent fit to the integrated light profiles of our models. We describe our technique in more detail in the Appendix. Finally we calculate the 3D central luminosity density, $\rho_{\rm c}$ (in units of $L_\odot/{\rm pc}^3$) within two different fractions of the core radius, $0.1\,r_{\rm c}$ and $0.25\,r_{\rm c}$. For comparison, we have also calculated

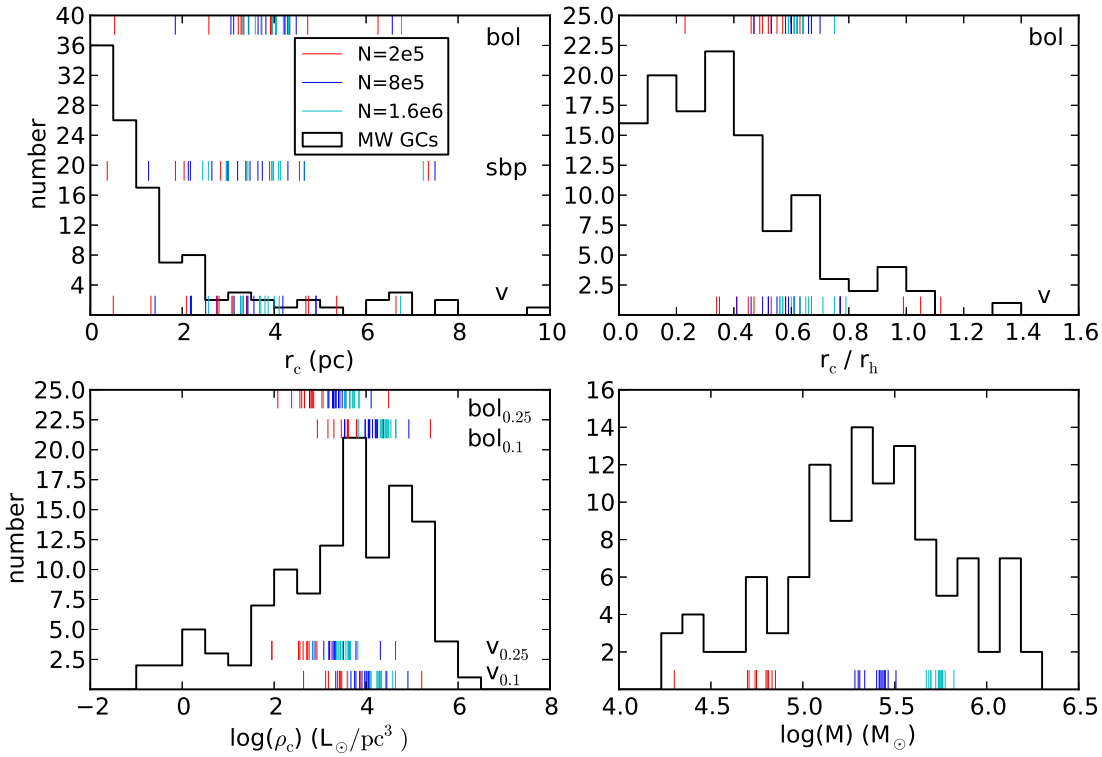

Fig. 10.— Comparison of observable properties for MW GCs and for our models. The MW data are taken from the Harris 1996 catalog (2010 edition), excluding the masses, which are from Gnedin & Ostriker 1997. The histograms show the distribution of core radii, r_c, the ratio of core to half-light radius, $r_c\,/\,r_h$, the central luminosity density, ρ_c, and total cluster mass, M, for the Milky Way GCs (Harris). The ticks show the calculated values of the same quantities for our models. The colors indicate the initial value of N. For quantities that depend on *light* (all of the above, except for M), we have calculated the quantities with at least two different methods, which are represented by the different sets of ticks at the bottom, center, or top of the plots. For r_c and r_h, the ticks on the bottom and top are calculated using the cumulative luminosity function using visual or bolometric luminosities, respectively. The ticks across the middle of the plot of r_c show the values as calculated from the surface brightness profile. For ρ_c, the bottom set of ticks shows the luminosity density calculated in the visual band within either 0.1 r_c or 0.25 r_c, and the two sets of ticks at the top of the panel represent the same quantities as derived from the bolometric luminosities. M is simply the sum of all the masses in the cluster. Our clusters agree well with MW GCs in terms of ρ_c and M, but our measured values for r_c and r_c/r_h fall on the high end of the distribution. The three low-N models that dissolved prior to 12 Gyr are excluded from these figures.

r_c using the bolometric luminosities output by our code, and from a SBP constructed for each of our models using a technique similar to that in Noyola & Gebhardt (2006). We find that the different techniques produce reasonable agreement, and we do not find any systematic bias in the values obtained via these three different methods. We show the cumulative luminosity profiles and SBPs for our six representative models in the Appendix. The observable properties for all models are given in Table 4.

In Figure 10 we compare r_c, r_c/r_h, ρ_c, and M_{tot} for our models to the actual values observed in MW GCs. All the Galactic GC data is taken from the Harris (1996) catalog (2010 edition),

except for the total cluster mass, which is from Gnedin & Ostriker (1997). The properties of the MW GCs are represented as histograms, and the colored tick marks indicate the final values for our models. Our $N = 8 \times 10^5$ models produce final clusters with roughly the median GC mass of about $10^5\,M_\odot$, and with our three different choices for N, the models span most of the range of MW GC masses. To model the largest MW clusters, we will have to extend our initial N to larger values. Our central densities also agree well with the bulk of the MW clusters, with the majority of our clusters at $\rho_c \sim 10^3 - 10^5\,L_\odot/pc^3$. We miss the very high and very low density tails of the distribution, but with larger and smaller initial N, and possibly other variations in our parameters, we would expect to be able to populate these regions.

We have the most trouble matching the core radius distribution of the MW GCs. We have a deficit of models with small cores ($r_c < 1$), which is where the bulk of MW GCs fall. Only one of our models, `n2-B`, has r_c less than a parsec ($r_c = 0.5$ pc). This happens to be the one model that manages to get rid of nearly all its BHs, which is the low-N cluster that starts out very compact ($R_v = 1$ pc). The core radii for our models do span almost the full range of values occupied by the MW GCs, although we would still like to see more models represented in the $r_c < 1$ pc region. Instead, most of our models have core radii between about 2–5 pc. The relatively large core radii measured also cause our r_c/r_h values to fall on the high end of the distribution, although our models span a significant fraction of the range occupied by MW clusters, except for $r_c/r_h < 0.3$.

Although it is not apparent from Figure 10, we can see in Table 4 that there are few correlations between cluster initial conditions and final core radii. Again we see the impact of the initial virial radius, in that the final core radius scales with the initial virial radius, across all models. We also notice a slight trend of clusters with smaller R_G and higher Z having slightly smaller cores. This would be expected in models with *either* a smaller R_G, which are more tidally truncated, and hence kept more compact, *or* with higher Z, since they produce lower-mass BHs, which have less of an impact on the cluster, and therefore allow the cores to contract more than when more massive BHs are present. We do not find any significant correlation between core radius and binary fraction. The final overall binary fractions (see Table 2) are, in most cases, similar to the initial values, while in a few of our models the *core* binary fraction, $f_{b,core}$, increases over time. This result is in agreement with numerical calculations by Fregeau et al. (2009), and is attributed to an imbalance of mass segregation of binaries into the core, and destruction of binaries through strong dynamical encounters (mass segregation wins out). In Figure 11, we show the time evolution of the overall binary fraction and the binary fraction within the 10% and 50% Lagrange radii for two models that display contrasting behavior. In model `n2-B` (top panel), the inner binary fraction increases steadily over time starting at around 1 Gyr, at which point the cluster has already ejected about 42% of its BHs; 85% of the BHs are ejected by 6 Gyr. Once the bulk of the BHs, especially the most massive ones, are lost, normal stellar binaries, which are much less massive than typical BHs, finally begin to segregate inward. By the end of the simulation, the binary fraction within the 10% mass bin has more than doubled. Moreover, the 50% and the overall binary fractions begin to increase in the last few Gyr. This is likely because of significant tidal stripping on this low-mass

Table 4. Observational quantities for all final models.

model	bolometric				visual				SBP
	r_c (pc)	r_h (pc)	r_c/r_h	$\log_{10}(\rho_c)$ ($M_\odot$/pc^3)	r_c (pc)	r_h (pc)	r_c/r_h	$\log_{10}(\rho_c)$ ($M_\odot$/pc^3)	r_c (pc)
n2w2rg2	2.43	3.18	0.76	3.59	1.36	3.13	0.43	3.77	2.9
n2w2rg8	3.22	6.19	0.52	3.62	3.4	4.41	0.77	3.38	3.01
n2w2rg20	3.34	6.85	0.49	3.54	2.09	5.16	0.41	3.47	1.85
n2w5rg2	2.98	3.88	0.77	3.69	2.65	3.37	0.78	3.9	2.86
n2w5rg8 †	3.3	6.54	0.5	3.6	4.75	4.24	1.12	3.59	3.0
n2w5rg20	3.28	7.15	0.46	3.59	3.1	5.88	0.53	3.44	3.9
n2w7rg2	2.92	3.88	0.75	3.9	2.36	3.38	0.7	4.09	2.13
n2w7rg8	3.72	7.08	0.53	3.8	2.8	6.01	0.47	3.87	4.55
n2w7rg20	4.29	7.82	0.55	3.3	2.75	6.14	0.45	3.18	2.84
n2-A	4.73	7.47	0.63	3.17	6.65	6.69	0.99	2.64	3.39
n2-B †	0.53	2.26	0.23	5.4	0.5	1.5	0.34	5.21	0.37
n2-C	6.26	10.41	0.6	2.94	5.36	9.19	0.58	3.12	7.35
n2-D	3.92	6.86	0.57	3.46	4.69	4.48	1.05	3.42	3.38
n2-E	2.58	5.43	0.47	3.79	1.32	3.77	0.35	4.07	2.04
n8w2rg2	3.06	4.96	0.62	4.38	2.51	3.99	0.63	4.45	2.18
n8w2rg8	3.82	6.36	0.6	4.14	3.33	5.73	0.58	4.0	2.99
n8w2rg20	3.95	6.86	0.58	4.07	3.13	6.03	0.52	3.75	3.65
n8w5rg2	3.44	5.23	0.66	4.21	2.2	4.21	0.52	4.02	3.21
n8w5rg8 †	3.73	6.25	0.6	4.2	2.18	5.35	0.41	4.29	2.97
n8w5rg20	4.04	6.91	0.59	4.08	3.56	6.04	0.59	3.91	4.3
n8w7rg2	3.65	5.47	0.67	4.23	3.41	4.44	0.77	4.05	2.13
n8w7rg8	4.04	6.9	0.59	4.05	3.27	6.59	0.5	3.86	3.0
n8w7rg20	4.48	7.45	0.6	3.98	4.91	6.39	0.77	3.67	3.74
n8-A	4.34	7.17	0.6	3.98	4.19	6.24	0.67	3.78	3.47
n8-B	1.85	3.94	0.47	4.93	1.41	3.05	0.46	4.91	1.27
n8-C	6.57	9.45	0.7	3.53	4.91	8.03	0.61	3.34	7.5
n8-D	4.23	6.65	0.64	4.05	3.43	5.66	0.61	3.97	4.66
n8-E †	3.12	5.88	0.53	4.25	2.76	4.99	0.55	4.29	2.65
n16w2rg2	3.3	5.12	0.64	4.65	3.27	4.34	0.75	4.58	2.57
n16w2rg8	3.72	6.02	0.62	4.49	3.12	5.55	0.56	4.33	3.39
n16w2rg20	3.96	6.47	0.61	4.41	3.3	5.76	0.57	4.33	4.1
n16w5rg2	3.34	5.25	0.64	4.64	2.57	4.48	0.57	4.64	2.96
n16w5rg8	4.03	6.28	0.64	4.43	3.71	5.64	0.66	4.24	3.99
n16w5rg20	4.25	6.92	0.61	4.36	3.87	6.46	0.6	4.29	3.43
n16w7rg2 †	3.59	5.63	0.64	4.54	3.07	4.85	0.63	4.42	2.44
n16w7rg8	4.31	6.74	0.64	4.34	4.11	6.14	0.67	4.11	4.65
n16w7rg20 †	4.32	7.07	0.61	4.31	3.68	6.52	0.56	4.09	4.14
n16-A	4.2	6.76	0.62	4.36	3.8	6.23	0.61	4.28	3.97
n16-B	2.07	4.08	0.51	5.11	1.59	3.31	0.48	5.01	1.65
n16-C	6.77	8.97	0.75	3.84	6.75	8.5	0.79	3.6	7.24
n16-D	4.05	6.28	0.64	4.44	4.0	5.59	0.71	4.24	3.95
n16-E	3.45	5.82	0.59	4.47	3.33	5.12	0.65	4.32	3.0

Note. — Calculations are described in Section 4.5. Columns 2–5 show the core radius (r_c), half-light radius (r_h), r_c/r_h, and the 3D luminosity density ($\log_{10}(\rho_c)$) calculated using the bolometric luminosities of stars as determined by BSE, while columns 6–9 show the same four quantities calculated using V-band luminosities (as described in the text). The last column shows the core radius as calculated from the SBP, also using V-band magnitudes. All radii are in units of parsec. The central luminosity density, ρ_c, is given in units of $L_{\odot,x}$/pc^3, where x is either the Sun's bolometric or V-band luminosity, in the two respective calculations.

cluster ($M_{\rm cl} \approx 5.6 \times 10^4 M_\odot$ at 12 Gyr), which will preferentially remove single stars, now that the binaries have started to segregate inward.

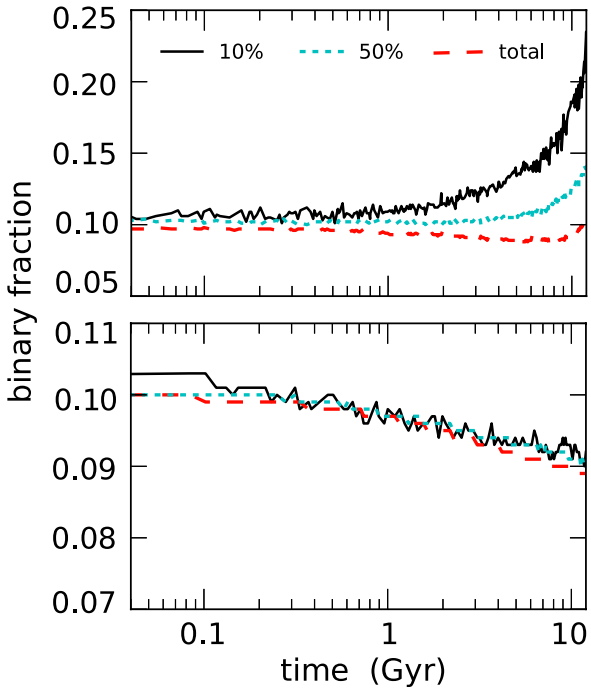

Fig. 11.— Binary fraction within the 10% and 50% Lagrange radii (solid black, dotted cyan, respectively) and the overall binary fraction (dashed red) as a function of time, for two different models, both starting with an initial binary fraction of 10% (note that what we call the initial binary fraction corresponds to *hard* binaries only; for example, for an initial hard binary fraction of 10%, the true binary fraction would be more like 20%). The top panel shows binary fractions for model `n2-B` and the lower panel shows model `n16w7rg20` (note the different scales on the y-axes). In model `n2-B` the binary fraction within the 10% Lagrange radius increases continuously with time, since with the bulk of its BHs lost within a few Gyr, primordial binaries (which are much less massive than typical BHs) can finally segregate into the central region of the cluster. The binary fraction within the half-mass radius remains fairly constant, while the overall binary fraction actually decreases slightly, until the last few Gyr, when the binary fraction starts to increase everywhere. Model `n16w7rg20` shows very different behavior, with its binary fraction decreasing everywhere over the entire simulation. Here we do not see an increase in the inner binary fraction, which may have to do with heating by the significant population of BHs retained all the way to 12 Gyr, which can quench the mass segregation of binaries.

We do not, however, see the trend of increasing core binary fraction in all models. In the lower panel of Figure 11, we show the evolution of the binary fractions for model `n16w7rg20`, all of which actually decrease with time, even within the central 10% Lagrange radius. In fact, in many of our larger-N models, or in clusters that have longer relaxation times for other reasons (e.g., larger virial radius), the trend of increasing central binary fraction is less significant or not present at all (on the timescale of the simulations). We expect the timescale for segregation of binaries to scale with relaxation time, but in our models it may have more to do with the presence of large numbers of BHs. As discussed by Mackey et al. (2008), the heating caused by a retained population of BHs can quench mass segregation of other objects (e.g., binaries) that would have otherwise experienced

significant mass segregation within a few Gyr. This is similar to the case of an intermediate-mass BH quenching mass segregation by scattering stars out of the core (e.g., Baumgardt et al. 2004; Gill et al. 2008). As long as the BHs are dominating the central dynamics, as is the case for most of our models, they seem to play a role in preventing segregation of binaries into the core.

Excluding the clusters that dissolved within a few Gyr, we find an overall anticorrelation between final core binary fraction and cluster mass (see Table 2), a trend that has been observed in MW GCs (Milone et al. 2012), as well as in the simulations of Fregeau et al. (2009) and Sollima (2008). Sollima (2008) suggest that this could be related to the fact that cluster mass and binary destruction efficiency both have the same dependence on cluster density and velocity dispersion. In our models, the trend may be due to a combination of multiple effects, including both heating (scattering) by stellar BHs and destruction of binaries in the core. Milone et al. (2012) measure core binary fractions $f_{\rm b} \lesssim 10\%$ for most MW clusters observed in the study, and we find that starting with initial binary fractions of 10%, our final core binary fractions too remain around 10% (typically between 9-12%, excluding dissolved clusters). Starting with a binary fraction of 50% yields final binary fractions that are much larger than those observed in GCs, but these models served as limiting cases to allow us to study the effect of binary fraction on the evolution of clusters with BHs.

5. Discussion and Conclusions

5.1. Summary of Results

Our goal here was to study the evolution of massive star clusters that initially retain most of their BHs in order to see whether it is possible for many BHs to remain after $\sim 10\,{\rm Gyr}$ and still have cluster properties consistent with those of MW GCs. Most of our clusters do indeed retain many BHs at the end of the simulations (up to $\sim 10^3$, for initial N from $2 \times 10^5 - 1.6 \times 10^6$), but the agreement with observable properties of MW GCs is not perfect. Qualitatively, all of our models evolve quite similarly, at least during the first few Gyr. The BHs quickly become very centrally concentrated, but, as a whole remain spread out over about a parsec in radius, similar to the innermost 10% of the non-BH mass. At the very center, the most massive BHs drive repeated core oscillations where a few tens of BHs collapse into a cusp, but then promptly re-expand via their own dynamics after forming three-body binaries. Single and binary BHs are ejected over time, with the most massive BHs being ejected first, followed by the less massive ones. As this happens, the remaining population of lower-mass BHs becomes less efficient at driving deep core collapses and the outer envelope of the oscillating central 1% BH mass slowly expands. This results in a lower central density and a gradual slowing of both the interaction rate and the BH ejection rate. While most models still have a significant population of $5 - 15\,M_\odot$ BHs at the end, we find that this depends sensitively on the initial conditions, in particular quantities that have the potential to significantly modify the cluster relaxation time, such as N and $R_{\rm v}$. Clusters with shorter relaxation

times (lower N, smaller $R_{\rm v}$) process their BHs more quickly, and therefore end up retaining smaller fractions of their initial BH populations by 12 Gyr. The mass of the most massive bound BH depends on the extent to which the BHs have been depleted. Model `n2-B` has the smallest N (2×10^5) and $R_{\rm v}$ (1 pc), and therefore the shortest relaxation time of all, and it retains just 9 BHs at 12 Gyr (about 2% of the initially retained BHs). Similarly, models `n8-B` and `n16-B` (larger N, but $R_{\rm v} = 1$ pc) retain the fewest BHs among other models with the same N.

Our models have final binary fractions that agree very well with observation. The total masses and luminosity densities for our models also fit well within the parameter space of observed MW clusters. Our final core radii, however, are for the most part too large to represent the bulk of MW clusters, although they do fall along the extended tail of the distribution. Like the dynamics of the BHs, the final core radii too are affected significantly by the initial virial radius. All models with $R_{\rm v} = 2$ pc have final core radii between $3 - 5$ pc, and those with $R_{\rm v} = 4$ pc have even larger cores ($6 - 7$ pc), regardless of N. The only models to eventually contract down to core sizes smaller than 2 pc are the three that *start* much more compactly with $R_{\rm v} = 1$ pc. These models all reach a point at which the BHs are providing so little energy that the cluster as a whole stops expanding, or in the case of model `n2-B`, actually starts contracting (see Figure 2), as the remaining low-mass BHs start to lose their dominance at the cluster center. In the last few Gyr of evolution in model `n2-B` the BHs become more and more integrated with the rest of the cluster, and finally the cluster core (i.e., the *observational* core, composed of luminous stars) starts to contract, resulting in a final core size of just 0.5 pc. This model has a mass of only $2 \times 10^4\,M_\odot$ at 12 Gyr, placing it at the very bottom of the MW GC mass distribution. In fact, the three most compact clusters lose mass at a faster rate overall than the comparable model with larger $R_{\rm v}$, and also end with fewer BHs and smaller cores, indicating that BH evaporation seems to be tied very closely to *cluster* evaporation. However, models `n8-B` and `n16-B` each have about the same final mass as the model `n8w5rg2` and `n16w5rg2`, respectively (which have $R_{\rm v} = 2$ pc, but smaller tidal radii) yet being more compact, they still eject their BHs more efficiently and therefore achieve smaller core sizes in the end.

Each of our models forms and ejects many BH binaries over the course of their evolution, but the majority of the BHs, both retained and ejected, are single BHs. Most of the ejected binaries are BH–BH, but some BH–non-BH binaries are ejected as well. The number of ejected BH binaries, their properties at ejection, and therefore the number of subsequent BH–BH mergers (inside and outside of the clusters) depend primarily on N and $R_{\rm v}$. We produce many BH–BH mergers (more than 4000 in total), with at least one merger produced in each cluster. Roughly 60% of the ejected BH–BH binaries actually merge within a Hubble time (we do not calculate this fraction for retained BH–BH binaries because their properties are still being modified by dynamics). Since our models do not yet show great agreement with all relevant properties of Galactic GCs, we cannot yet make any reliable quantitative predictions about the numbers of interesting BH binary systems in our Galaxy, or other similar galaxies.

5.2. Uncertainties and Comparison to Other Studies

Breen & Heggie (2013) were the first to suggest that the dynamics of a population of BHs is actually regulated by the *cluster*, and that for this reason BHs can be retained for much longer than previously thought. In their simplified two-component cluster models they found that the BHs behave such that they meet the energy needs of the cluster, similar to the way that primordial binaries balance energy flow during the binary-burning phase (Fregeau & Rasio 2007; Gao et al. 1991). Earlier studies (Mackey et al. 2008; Merritt et al. 2004) have demonstrated that the interactions (and subsequently the ejections) of a segregated population of BHs can inject enough heat to cause significant core expansion in clusters. Breen & Heggie (2013) find that some point, however, there are too few BHs to balance the energy lost via relaxation, and only then can the cluster finally approach the phase that the authors call *second core collapse*, to distinguish it from the initial BH-driven collapse (*second* core collapse therefore refers to what is usually just called *core collapse*). If the *cluster* drives the rate of energy flow, we should not expect the BHs to evaporate within a few cluster relaxation times. Our results agree with this basic picture, and we see this very behavior play out in our model `n2-B`, which is actually approaching the second core collapse phase by the end of the simulation. All of our models display many deep collapses of a small number of BHs, but the formation of three-body binaries and their subsequent interactions ultimately power the re-expansion of the cusp. We find that the BHs actually spend *most* of their time in the *uncollapsed* state, which also helps to explain how it is possible for BHs to remain in clusters for so long. The BHs *try* to decouple via the Spitzer instability, but their own dynamics ensures that they always re-couple to the cluster very quickly.

Heggie & Giersz (2014) also discuss the dependence of BH retention on relaxation time by comparing models of four clusters with very different initial conditions (modeled after M4, NGC 6397, 47 Tuc and M22). The M4 and NGC 6397 models both have short relaxation times, and although they retain nearly all the BHs *initially*, they eject almost all of them within 12 Gyr. In contrast, the 47 Tuc and M22 models start with only 10% of the formed BHs initially, yet given their longer relaxation timescales most of these BHs still remain at 12 Gyr. The difference, they explain, is that the models are in different dynamical states: the former two models have reached the second core collapse phase, while the latter two are far from it. They predict that clusters with long relaxation times are more likely to still contain many BHs at present. We have shown that this is true for our models as well, but to make the point more clearly we show in Figure 12 the relationship between the final fraction of BHs retained and the final number of bound stars for our models. This shows that the trend predicted by Heggie & Giersz (2014) holds roughly for a wide range of initial conditions, although the variety of initial conditions also leads to the large amount of scatter.

While these studies (as well as our own) agree that BH dynamics is regulated for the most part by the cluster, there are still uncertainties about initial BH populations in GCs that may impact the precise evolutionary timescale for BH evaporation, and therefore predictions for present-day clusters. The BH mass spectrum (derived from the remnant-to-progenitor mass relationship and the upper end of the stellar IMF) is somewhat uncertain. Since the most massive BHs are ejected first,

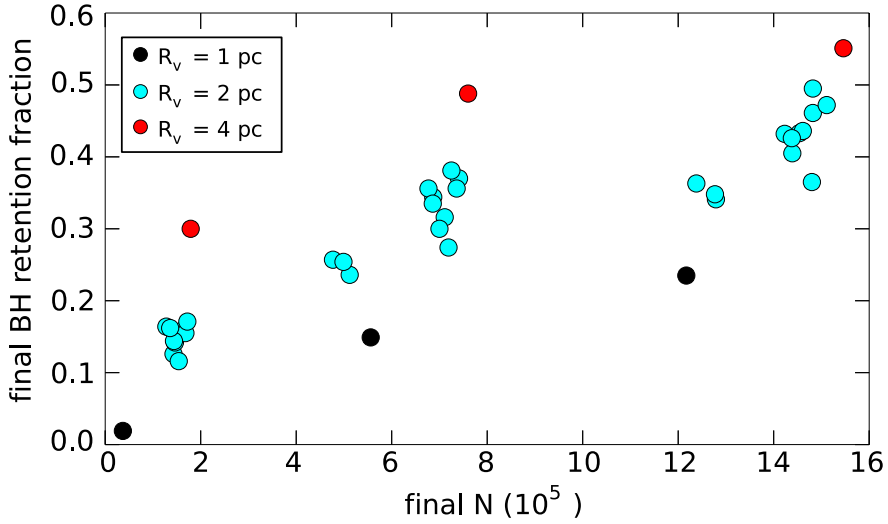

Fig. 12.— Relationship between final BH retention fraction and final N for all models that survive to 12 Gyr. The different colors indicate the initial virial radius. The trends of increasing BH retention fraction with N and with R_v are expected since the relaxation time depends on N. Clusters with either smaller N or smaller R_v have shorter evolutionary timescales, and are therefore in a later dynamical state at 12 Gyr, so they have ejected larger fractions of their BHs, as well as lost more mass overall.

and the impact of BHs on the cluster lessens with time as BHs are ejected, the BH mass spectrum could significantly affect the long-term evolution of BHs and clusters. Another key uncertainty is the magnitude of birth kicks for BHs. Studies attempting to constrain BH kick strengths using observations of BH XRBs have led to mixed conclusions. Repetto et al. (2012) suggested that large kicks (similar to those of NSs) were necessary to explain the spatial distribution of BH XRBs in the Galaxy, while other studies have found that lower natal kick velocities better explain the properties of at least some specific systems (e.g., Willems et al. 2005; Wong et al. 2012). There are also competing theories for the origin of these kicks (e.g., neutrino-driven versus supernova-driven) which lead to different predictions for the magnitudes that we should expect for BHs (see summary in Janka 2013). Janka (2013) presented a new kick model that might explain how BHs could acquire kicks similar to those of NSs. The model suggests that asymmetric supernova ejecta could lead to an acceleration of the remnant BH gravitationally in the same direction as the initial kick, in which case the kick momentum *grows* with BH mass. Recent models of M22 presented in Sippel & Hurley (2013) and Heggie & Giersz (2014) found good agreement with observable properties of M22 by starting with very small initial retention fractions (10%, or about 50 BHs), under the assumption that BHs receive the same kicks as NSs. For comparison, we have repeated 3 simulations (`n2w5rg8`, `n8w5rg8`, and `n16w5rg8`), except we allowed BHs to receive kicks identical to those of NSs (kick chosen independent of mass or fallback). As expected, we find that very few BHs are retained initially (0, 6, and 31, for the three models, respectively), and they have little effect on their host clusters. It seems that such a small number of BHs cannot power the deep collapses that we have seen in the simulations described in this work. This also helps to explain how these models that retained just 6 and 31 BHs initially, still managed to keep 5 and 19 of them (respectively) all the

way to 12 Gyr, since BH ejections tend to occur predominantly during the deep collapse phases, which are absent from the models with very few BHs. However, since the goal of this work is to better understand the evolution of clusters that retain most of their BHs initially, and to determine to what extent these clusters resemble our Galactic GCs, we have chosen to focus on the effects of varying *only* the initial conditions of the cluster models as a whole, and have left the initial BH populations fixed, except for the differences that arise naturally from different choices for cluster parameters. The effect of BH kicks and the BH mass spectrum will be the topic of a future study.

With the growing evidence for BH XRBs in old GCs, it would also be interesting to use our models to predict the numbers and properties of BH XRBs in GCs. However, we cannot trust our simple treatment of binary stellar evolution to predict the behavior of these binaries. This would require more focused binary evolution and mass transfer modeling of specific systems that form in our cluster models. A very crude analysis of the entire population of retained BH binaries with non-compact companions at 12 Gyr indicates that at least some of these systems (28, or about 13%) could potentially be interesting X-ray sources at present. Since we use the standard "sticky sphere" approximation for physical collisions, our code is also not capable of predicting detailed outcomes of collisions between BHs and non-compact stars. Our standard treatment leads effectively to the entire mass of the colliding objects to be entirely and immediately accreted onto the BH, ignoring completely any feedback effects (which could lead to significant mass loss) or the finite timescale of the accretion flow. Our code can, however, predict the *rates* of these collisions and as a quick test we have checked how many collisions occur between BHs and non-degenerate stars in one of our large-N models (`n16w5rg8`). In total there were 45 direct collisions involving a BH and a non-degenerate star, which occurred via different kinds of interactions: 23 occurred as direct S-S collisions, 18 during strong B-S interactions, and 4 during B-B interactions. Most of these collisions were with main-sequence stars (40), but there were also a few collisions with giants (5), which, if treated in more detail would have likely led to the formation of a compact BH–WD binary remnant (Ivanova et al. 2010). About half of the collisions happen within the first Gyr, and the rate declines after that. We also see 21 evolutionary mergers between a BH and a non-degenerate star, which occurred during binary stellar evolution rather than during dynamical encounters. All of these mergers were with MS stars, and they all occurred within the first 13 Myr. We have not yet studied the details of these collisions and mergers, but it would be interesting to look at their properties, such as impact parameter and stellar masses, and then predict the possible observable outcomes of such events, as they could produce transient sources that would be detectable by surveys such as LSST (LSST Science Collaboration et al. 2009).

Perhaps most importantly, on the computational side, since we find that cusps involving a few tens of BHs form repeatedly in our models, we must ask whether an orbit-averaged MC approach can model this dynamical behavior accurately. In particular, for a small-N decoupled subsystem, the relaxation and dynamical timescales can become comparable, in which case the Fokker-Planck approximation, a key assumption in the MC technique, breaks down. Furthermore, such a small number of particles makes the estimation of local averages highly susceptible to Poisson fluctuations,

which directly influences the accuracy of all dynamical calculations. The direct N-body technique does not suffer from these issues, and so it can handle the dynamics of a small-N system quite naturally. This is most likely responsible for the difference in core radius between the two methods that was noted in Figure 1. In a BH-driven collapse, the small number of massive particles interact on a much shorter timescale than our relaxation timestep can resolve. In order to address this, we are currently developing a new technique that will allow us to model the dynamics of these deep collapses more accurately. This hybrid N-body/Monte Carlo technique integrates the dynamics of the BHs (or other massive particles) directly with an N-body integrator, while the majority of lower-mass stars in the halo and core interact via the two-body relaxation of the MC approach. Preliminary results indicate that this technique achieves similar speed to a pure MC simulation while producing core radii that agree with results observed in full N-body simulations (Rodriguez et al. 2014).

5.3. Conclusions

Starting with reasonable initial conditions describing young star clusters we have presented many simulations of GCs containing populations of hundreds to thousands of BHs. Without any fine tuning of parameters, we find that our models have present-day observable properties that are consistent with the MW GCs, although our core radii are slightly large.

Our main conclusion is that *if* most BHs are retained initially, it seems that the only way to still eject most or all BHs by $\sim 12\,\mathrm{Gyr}$ is to start with very compact clusters. If clusters can eject enough BHs, then the core can finally begin to contract, producing final core radii that may be in better agreement with those observed in MW clusters. Most of our models, on the other hand, retain significant numbers of BHs all the way to 12 Gyr (typically $\approx 50-100$ for our lowest-N models, and $\approx 1000-2000$ for our largest-N models), and have rather large cores (typically about 2–5 pc). We confirm that the BH evaporation timescale is set by the cluster evolutionary timescale as suggested by Breen & Heggie (2013) and Heggie & Giersz (2014). We find that the BHs drive deep core oscillations during which a small number of BHs can form a steep cusp, but these always re-expand and re-mix with the other stars very quickly, and the result is that most of the time the BHs are in their uncollapsed state, well mixed with other stars. We suggest that this may explain why the BHs mostly avoid the Spitzer instability, and hence why they can be retained for much longer timescales than previously thought.

It will be important to test the effect of uncertain stellar parameters, especially those pertaining to the BH populations, such as BH birth kick magnitudes and the BH mass – progenitor mass relationship, which we have not explored in this study. These parameters will undoubtably affect the subsequent dynamics of the BHs and the clusters as a whole, and may therefore also change the predictions for BH retention. If it turns out that BHs do indeed get kicks of the same magnitude as NSs and so at most only $\sim 10\%$ are retained initially, then the very compact initial conditions might not be necessary to produce small cores by ~ 12 Gyr, since there would be far fewer BHs to

eject before the core could start to contract.

In order to derive the proper BH–BH merger rate for MW-equivalent galaxies (and the corresponding predicted LIGO detection rate) we will first need to run additional simulations in order to fill in the gaps where we currently have poor coverage in the parameter space of observed MW GCs. We will then be able to do a detailed statistical calculation that weighs the contribution from each of our models according to how well their properties match the MW population. This calculation will be the topic of a forthcoming paper (Rodriguez et al., in preparation).

A. Calculation of Observational Core Radius

To make a SBP requires the stars to be binned radially. The bins should be small enough in radius that the core is resolved. The tradeoff is that small bin sizes increase the random noise, since a single bright star can dominate the light for an individual bin, introducing large bin-to-bin variations. To get around this, observers generally remove the brightest stars before calculating the SBP (Noyola & Gebhardt 2006) based on a somewhat arbitrary choice of a magnitude cutoff. A detailed discussion and comparison of various techniques can be found in Noyola & Gebhardt (2006).

To avoid the complications of binning, we have chosen to use a new technique for calculating the core radius. Our technique involves fitting a king model to the *cumulative* luminosity function, which is much smoother than the luminosity density (or surface brightness profile) because it does not require us to bin the stars. We start with the analytic approximation to the King model density profile (Equation 13 from (King 1962)),

$$\Sigma(r) = \frac{\Sigma_o}{1 + (r/r_{\rm c})^2}, \tag{A1}$$

where Σ_o is the central 2D surface density and $r_{\rm c}$ is the King core radius. We then integrate this equation over the surface area out to some distance r, so that it is now represents the *cumulative* luminosity as a function of r,

$$L_{tot}(r) = \pi \Sigma_o r_{\rm c}^2 \log\left(1 + (r/r_{\rm c})^2\right). \tag{A2}$$

Finally, we fit this equation to the cumulative luminosity profile for each of our models to find the best values for Σ_o and $r_{\rm c}$.

All core radii given in columns 2 and 6 of Table 4 are calculated using this technique, based on either the bolometric or the V-band luminosities. We show the cumulative luminosity profiles and the SBPs for a sample of six of our models in Figure 13.

We thank the anonymous referee for several suggestions that improved this work. This work was supported by NSF Grant AST–1312945 and NASA Grants NNX09AO36G and NNX14AP92G at Northwestern University. MM acknowledges support from an NSF GK-12 Fellowship funded through NSF Award DGE- 0948017 to Northwestern University. FAR acknowledges the hospitality of the Aspen Center for Physics, supported by NSF Grant PHY-1066293. All computations were performed on Northwestern University's HPC cluster Quest.

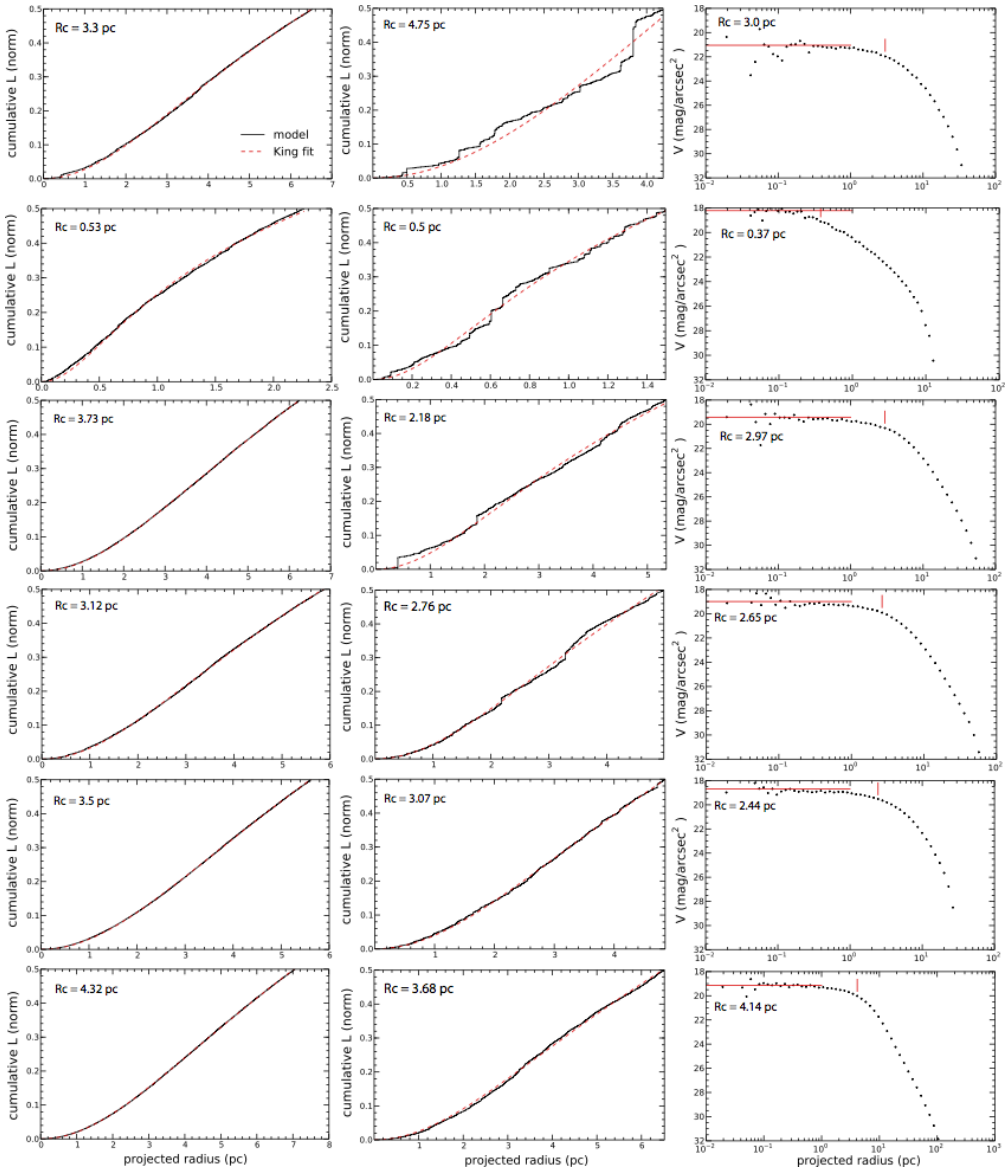

Fig. 13.— Core radii calculations for the six models shown in Figure 2. The left panels show the cumulative luminosity profile calculated from the bolometric luminosities (solid black curve) and the King fit to the model (red dashed curve). The resulting r_c obtained using our new technique (as described in Section 4.5 and the Appendix) is given on each panel. The center panels show the same thing, but using V-band luminosities. On the right panels we show the V-band SBP for each model with a vertical red tick mark to indicate the location of r_c, the point at which the surface luminosity density drops to half the central value. The horizontal red line indicates the central brightness. For simplicity we assume all clusters are at a distance of 8.5 kpc. This choice does not affect the core radius measurement, but it does affect the magnitude scale (y-axis), and therefore the numerical values here are somewhat arbitrary.

REFERENCES

Abadie, J. et al. 2010, Classical and Quantum Gravity, 27, 173001

Banerjee, S., Baumgardt, H., & Kroupa, P. 2010, MNRAS, 402, 371

Barnard, R., Garcia, M., Li, Z., Primini, F., & Murray, S. S. 2011, ApJ, 734, 79

Baumgardt, H., Makino, J., & Ebisuzaki, T. 2004, ApJ, 613, 1143

Belczynski, K., Kalogera, V., & Bulik, T. 2002, ApJ, 572, 407

Belczynski, K., Sadowski, A., & Rasio, F. A. 2004, ApJ, 611, 1068

Belczynski, K., Sadowski, A., Rasio, F. A., & Bulik, T. 2006, ApJ, 650, 303

Breen, P. G., & Heggie, D. C. 2013, MNRAS, 432, 2779

Casertano, S., & Hut, P. 1985, ApJ, 298, 80

Chatterjee, S., Fregeau, J. M., Umbreit, S., & Rasio, F. A. 2010, ApJ, 719, 915

Chatterjee, S., Umbreit, S., Fregeau, J. M., & Rasio, F. A. 2013, MNRAS, 429, 2881

Chernoff, D. F., & Huang, X. 1996, in IAU Symposium, Vol. 174, Dynamical Evolution of Star Clusters: Confrontation of Theory and Observations, ed. P. Hut & J. Makino, 263

Chomiuk, L., Strader, J., Maccarone, T. J., Miller-Jones, J. C. A., Heinke, C., Noyola, E., Seth, A. C., & Ransom, S. 2013, ApJ, 777, 69

Djorgovski, S., & Meylan, G. 1994, AJ, 108, 1292

Dominik, M., Belczynski, K., Fryer, C., Holz, D. E., Berti, E., Bulik, T., Mandel, I., & O'Shaughnessy, R. 2012, ApJ, 759, 52

Farr, W. M., Sravan, N., Cantrell, A., Kreidberg, L., Bailyn, C. D., Mandel, I., & Kalogera, V. 2011, ApJ, 741, 103

Fregeau, J. M., Chatterjee, S., & Rasio, F. A. 2006, ApJ, 640, 1086

Fregeau, J. M., Gürkan, M. A., Joshi, K. J., & Rasio, F. A. 2003, ApJ, 593, 772

Fregeau, J. M., Ivanova, N., & Rasio, F. A. 2009, ApJ, 707, 1533

Fregeau, J. M., & Rasio, F. A. 2007, ApJ, 658, 1047

Fryer, C. L., & Kalogera, V. 2001, ApJ, 554, 548

Gao, B., Goodman, J., Cohn, H., & Murphy, B. 1991, ApJ, 370, 567

Giersz, M., Heggie, D. C., & Hurley, J. R. 2008, MNRAS, 388, 429

Gill, M., Trenti, M., Miller, M. C., van der Marel, R., Hamilton, D., & Stiavelli, M. 2008, ApJ, 686, 303

Gnedin, O. Y., & Ostriker, J. P. 1997, ApJ, 474, 223

Grindlay, J. E., Heinke, C., Edmonds, P. D., & Murray, S. S. 2001, Science, 292, 2290

Harris, W. E. 1996, VizieR Online Data Catalog, 7195, 0

Harry, G. M., et al. 2010, Classical and Quantum Gravity, 27, 084006

Heggie, D., & Hut, P. 2003, The Gravitational Million-Body Problem: A Multidisciplinary Approach to Star Cluster Dynamics (Cambridge University Press)

Heggie, D. C. 1975, MNRAS, 173, 729

Heggie, D. C., & Giersz, M. 2014, MNRAS, 439, 2459

Hénon, M. H. 1971, Ap&SS, 14, 151

Hurley, J. R. 2007, MNRAS, 379, 93

Hurley, J. R., Pols, O. R., & Tout, C. A. 2000, MNRAS, 315, 543

Hurley, J. R., Tout, C. A., & Pols, O. R. 2002, MNRAS, 329, 897

Ivanova, N., Belczynski, K., Fregeau, J. M., & Rasio, F. A. 2005, MNRAS, 358, 572

Ivanova, N., Chaichenets, S., Fregeau, J., Heinke, C. O., Lombardi, Jr., J. C., & Woods, T. E. 2010, ApJ, 717, 948

Janka, H.-T. 2013, MNRAS, 434, 1355

Joshi, K. J., Nave, C. P., & Rasio, F. A. 2001, ApJ, 550, 691

Joshi, K. J., Rasio, F. A., & Portegies Zwart, S. 2000, ApJ, 540, 969

Kalogera, V., King, A. R., & Rasio, F. A. 2004, ApJ, 601, L171

King, I. 1962, AJ, 67, 471

King, I. R. 1966, AJ, 71, 276

Kroupa, P. 2001, MNRAS, 322, 231

Kulkarni, S. R., Hut, P., & McMillan, S. 1993, Nature, 364, 421

Lejeune, T., Cuisinier, F., & Buser, R. 1998, A&AS, 130, 65

LSST Science Collaboration et al. 2009, ArXiv e-prints, 0912.0201

Maccarone, T. J., Kundu, A., Zepf, S. E., & Rhode, K. L. 2007, Nature, 445, 183

——. 2011, MNRAS, 410, 1655

Mackey, A. D., Wilkinson, M. I., Davies, M. B., & Gilmore, G. F. 2008, MNRAS, 386, 65

Mennekens, N., & Vanbeveren, D. 2014, A&A, 564, A134

Merritt, D., Piatek, S., Portegies Zwart, S., & Hemsendorf, M. 2004, ApJ, 608, L25

Milone, A. P. et al. 2012, A&A, 540, A16

Morscher, M., Umbreit, S., Farr, W. M., & Rasio, F. A. 2013, ApJ, 763, L15

Noyola, E., & Gebhardt, K. 2006, AJ, 132, 447

O'Leary, R. M., Rasio, F. A., Fregeau, J. M., Ivanova, N., & O'Shaughnessy, R. 2006, ApJ, 637, 937

Pattabiraman, B., Umbreit, S., Liao, W.-k., Choudhary, A., Kalogera, V., Memik, G., & Rasio, F. A. 2013, ApJS, 204, 15

Peters, P. C. 1964, Phys. Rev., 136, B1224

Pooley, D. et al. 2003, ApJ, 591, L131

Portegies Zwart, S. F., & McMillan, S. L. W. 2000, ApJ, 528, L17

Repetto, S., Davies, M. B., & Sigurdsson, S. 2012, MNRAS, 425, 2799

Rodriguez, C., Pattabiraman, B., Chatterjee, S., Umbreit, S., Morscher, M., & Rasio, F. 2014, in prep.

Shih, I. C., Kundu, A., Maccarone, T. J., Zepf, S. E., & Joseph, T. D. 2010, ApJ, 721, 323

Sigurdsson, S., & Hernquist, L. 1993, Nature, 364, 423

Sippel, A. C., & Hurley, J. R. 2013, MNRAS, 430, L30

Sollima, A. 2008, MNRAS, 388, 307

Spitzer, Jr., L. 1969, ApJ, 158, L139

Strader, J., Chomiuk, L., Maccarone, T. J., Miller-Jones, J. C. A., & Seth, A. C. 2012, Nature, 490, 71

The Virgo Collaboration. 2014, ArXiv e-prints, 1408.3978

Trenti, M., Vesperini, E., & Pasquato, M. 2010, ApJ, 708, 1598

Umbreit, S., Fregeau, J. M., Chatterjee, S., & Rasio, F. A. 2012, ApJ, 750, 31

Verbunt, F., & Lewin, W. H. G. 2006, Globular cluster X-ray sources, ed. W. H. G. Lewin & M. van der Klis, 341–379

Watters, W. A., Joshi, K. J., & Rasio, F. A. 2000, ApJ, 539, 331

Willems, B., Henninger, M., Levin, T., Ivanova, N., Kalogera, V., McGhee, K., Timmes, F. X., & Fryer, C. L. 2005, ApJ, 625, 324

Wong, T.-W., Valsecchi, F., Fragos, T., & Kalogera, V. 2012, ApJ, 747, 111

This preprint was prepared with the AAS LaTeX macros v5.2.